

# Time-Resolved Optical Pump-Resonant X-ray Probe Spectroscopy of 4-Thiouracil: A Simulation Study

Yeonsig Nam,<sup>\*,†</sup> Francesco Montorsi,<sup>‡</sup> Daniel Keefer, Stefano M. Cavaletto, Jin Yong Lee,<sup>\*</sup> Artur Nenov,<sup>\*</sup> Marco Garavelli, and Shaul Mukamel<sup>\*</sup>



Cite This: <https://doi.org/10.1021/acs.jctc.2c00064>



Read Online

ACCESS |



Metrics & More

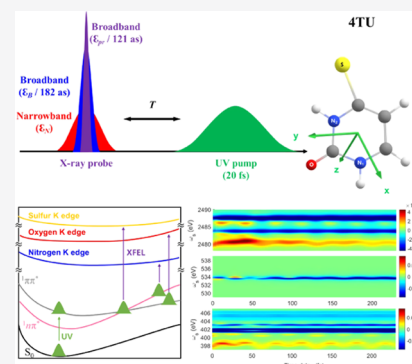


Article Recommendations



Supporting Information

**ABSTRACT:** We theoretically monitor the photoinduced  $\pi\pi^* \rightarrow n\pi^*$  internal conversion process in 4-thiouracil (4TU), triggered by an optical pump. The element-sensitive spectroscopic signatures are recorded by a resonant X-ray probe tuned to the sulfur, oxygen, or nitrogen K-edge. We employ high-level electronic structure methods optimized for core-excited electronic structure calculation combined with quantum nuclear wavepacket dynamics computed on two relevant nuclear modes, fully accounting for their quantum nature of nuclear motions. We critically discuss the capabilities and limitations of the resonant technique. For sulfur and nitrogen, we document a pre-edge spectral window free from ground-state background and rich with  $\pi\pi^*$  and  $n\pi^*$  absorption features. The lowest sulfur K-edge shows strong absorption for both  $\pi\pi^*$  and  $n\pi^*$ . In the lowest nitrogen K-edge window, we resolve a state-specific fingerprint of the  $\pi\pi^*$  and an approximate timing of the conical intersection via its depletion. A spectral signature of the  $n\pi^*$  transition, not accessible by UV–vis spectroscopy, is identified. The oxygen K-edge is not sensitive to molecular deformations and gives steady transient absorption features without spectral dynamics. The  $\pi\pi^*/n\pi^*$  coherence information is masked by more intense contributions from populations. Altogether, element-specific time-resolved resonant X-ray spectroscopy provides a detailed picture of the electronic excited-state dynamics and therefore a sensitive window into the photophysics of thiobases.



## INTRODUCTION

Pump-probe spectroscopy is the simplest nonlinear optical technique for monitoring the photoinduced excited-state dynamics in molecules.<sup>1,2</sup> It has been used with immense success to resolve ultrafast internal conversion (IC) and intersystem crossing (ISC) in pyrimidine nucleobases<sup>3–6</sup> and their thionated counterparts<sup>7–10</sup> by probing in the visible (Vis) and ultraviolet (UV) regime. In thio-nucleobases, one or more carbonyl oxygen atoms are substituted with sulfur atoms which strongly affects their photophysics. Thiouracils (Scheme 1a), i.e., the thionated form of the uracil nucleobase, undergo internal conversion (IC) from an optically bright  $\pi\pi^*$  state to a dark  $n\pi^*$  state mediated by a conical intersection (CoIn). The IC is followed by an ISC to form a long-lived triplet state with a high quantum yield, which facilitates applications as site-specific photoprobe for photodynamic therapy,<sup>11,12</sup> and as photoinduced cross-linkers.<sup>13,14</sup> The intermediate dark  $n\pi^*$  state of thiouracils has not been directly probed so far by UV–vis transient spectroscopy due to the low oscillator strength of its photoinduced absorption and emission.

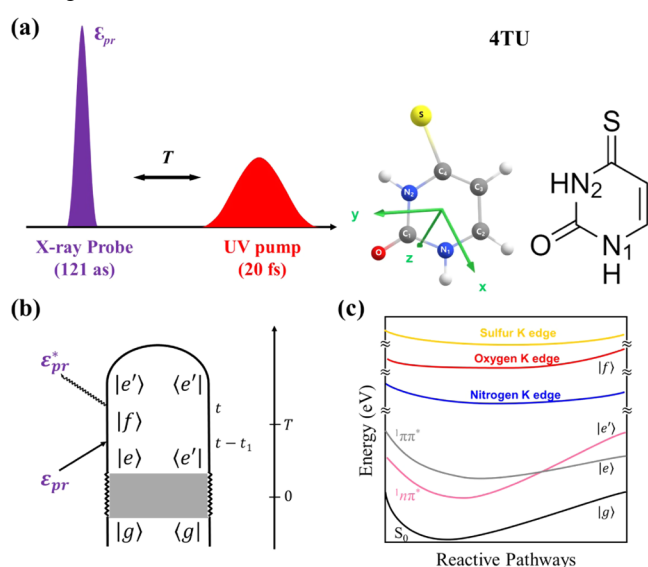
X-ray free-electron lasers (XFELs) light sources provide intense pulses at frequencies ranging from the XUV to the hard-X-ray regime<sup>15</sup> with high temporal, spectral, and spatial resolutions. XFEL-based probes, such as transient X-ray absorption (TRXAS) and photoelectron (TRXPS) spectroscopy,

<sup>16–18</sup> have been employed to monitor an electrocyclic ring-opening reaction,<sup>19</sup> intersystem crossing,<sup>20</sup> and the free evolution of molecules passing through CoIns<sup>21,22</sup> with sub-10 fs temporal resolution.<sup>23</sup> The unique capability of TRXAS to resolve transiently populated dark states has been demonstrated for the nucleobases uracil<sup>24</sup> and thymine<sup>25</sup>

Earlier we had proposed two off-resonant techniques for probing the passage through CoIns, namely, transient redistribution of ultrafast electronic coherences in attosecond Raman signals (TRUECARS) and time-resolved X-ray diffraction (TRXD), and employed to study the IC in 4-thiouracil (4TU).<sup>26</sup> TRUECARS keeps track of vibronic coherences, thereby providing the temporal and spectral profiles of the CoIn in a background-free manner. TRXD images the time-evolving electron charge densities, hence providing real-space images of charge densities at CoIns. These off-resonant techniques can be used universally to obtain snapshots of the passage through the CoIn but do not carry

Received: January 19, 2022

**Scheme 1.** (a) Pulse Configuration and Molecular Geometry of 4-Thiouracil; the 20 fs FWHM Gaussian Pump Creates a Population in the  $S_2$  ( $\pi\pi^*$ ) State. At Time Delay  $T$ , a Single Broadband X-ray Probe Pulse is Used; (b) Loop Diagram for the Optical Pump, X-ray Probe Signal. The Electronic Excited-State Dynamics is Monitored by the Weak Probe in the Presence of a Pump Pulse Initiating the Evolution of a Nonstationary State. An Incoming X-ray Pulse ( $\mathcal{E}_{\text{pr}}$ ) Excites a Molecule on a Ground/Valence Electronic Surface  $|e\rangle$  into a Core Level  $|f\rangle$  after Time Delay  $T$  Following an Initial Excitation into a Nonstationary State and Free Evolution Period (Gray Box). Then, Signal Field Emission is Stimulated by  $\mathcal{E}_{\text{pr}}^*$ .  $e = e'$  Gives Excited Absorption and Ground-State Bleach Signals, while  $e \neq e'$  Gives a Raman Signal. The Complete Diagram Rules Are Given in Ref 28 and the SI; (c) Energy-Level Scheme of the Measurement. Black, Pink, and Gray Colors Correspond to the Ground State,  $n\pi^*$ , and  $\pi\pi^*$  Valence States, and Blue, Red, and Yellow Colors Correspond to Nitrogen, Oxygen, and Sulfur K-Edges



information about the population evolution on the individual electronic states.

Here, we further address the  $\pi\pi^* \rightarrow n\pi^*$  IC in 4TU and present an ab initio computational protocol for obtaining element-sensitive core-to-valence spectroscopic signatures accessible through TRXAS using probe pulses resonant with either the sulfur, oxygen, or nitrogen K-edges. To this aim, we employ multiconfigurational wave function-based electronic structure methods optimized for core-excited electronic structure calculations combined with grid-based exact quantum dynamics in reduced coordinate space. The capabilities and limitations of the resonant technique are discussed. Specifically, for sulfur and nitrogen, we identify a pre-edge spectral window free from ground-state absorption background and rich with excited-state absorption features. In the nitrogen pre-edge window, we resolve clear  $n\pi^*$  signatures, which rise with a delay matching the  $\pi\pi^*$  lifetime. We demonstrate that coherences created during the CoIn passage remain hidden under the more intense contributions from populations, making TRXAS complementary to the TRUEARS technique, which is insensitive to population dynamics.

## COMPUTATIONAL PROTOCOL

**Optical Pump-Resonant X-ray Probe Signals.** A UV-vis pump brings the system into an optically bright valence excited state, or into a superposition thereof. A weak X-ray pulse then probes the nonadiabatic dynamics (Scheme 1a) at time delay  $T$ . The light-matter interactions and the evolution of the system can be represented diagrammatically by a loop diagram (Scheme 1b). The shaded area in the diagram represents an arbitrary excitation, which is then followed by the nonadiabatic dynamics (wavy lines). The left branch of the loop represents the time evolution of the ket wavepacket until the expectation value is taken at time  $t$ , whereas the right branch represents the time evolution of the bra wavepacket. After the interaction with the pump, the ket evolves in the valence manifold  $|e\rangle$  according to the propagator  $G_0(t - t_1)$ . At time  $t - t_1$ , an incoming X-ray pulse ( $\mathcal{E}_{\text{pr}}$ ) brings the molecule once again into the core-excited manifold  $|f\rangle$ . The core state has a very short lifetime, we thus neglect the nuclear dynamics during time  $t_1$  and the propagation is represented by a solid line. The second interaction with the probe ( $\mathcal{E}_{\text{pr}}^*$ ) at time  $t$  brings down the wavepacket into the valence state  $e'$ . The signal is finally calculated as the scalar product of the propagated ket and bra at time  $t$ . No interaction with the X-ray fields takes place in the right branch, and the bra evolves in the valence manifold from the initial time to  $t$  using the propagator  $G_0^\dagger(t)$ .

The X-ray probe-matter interaction Hamiltonian in the rotating-wave approximation is given by

$$H_{\text{int}} = -E(t) \cdot \mu^\dagger - E^*(t) \cdot \mu \quad (1)$$

The dipole moment operator reads

$$\mu = \sum_{ef} \mu_{ef} |f\rangle \langle e| \quad (2)$$

where  $\mu_{ef}$  is a lowering operator acting on the nuclear space, with index  $e$  running over the valence excited states and the ground state and  $f$  running over the core-excited states of the molecule. The complex probe electric field centered at time  $T$

$$E(t) = e\mathcal{E}(t - T)e^{-i\omega_0(t-T)} \quad (3)$$

has polarization vector  $e$ , envelope  $\mathcal{E}(t)$ , and central frequency  $\omega_0$ . We introduce the Fourier transform

$$E(\omega) = e\mathcal{E}(\omega - \omega_0)e^{i\omega T} \quad (4)$$

The pump-probe signal is defined as the change in the frequency-dispersed transmitted probe pulse, i.e., the time-integrated rate of change of the number of photons at the probe signal frequency  $\omega_s$ ,

$$S(\omega_s, T) = \int \left\langle \frac{dN(\omega_s)}{dt} \right\rangle dt \quad (5)$$

Here,  $N(\omega_s) = a^\dagger(\omega_s) a(\omega_s)$  is the number operator of a photon at the detected frequency  $\omega_s$ , with the associated Boson creation and annihilation operators,  $a^\dagger(\omega_s)$  and  $a(\omega_s)$ , respectively. Solving the Heisenberg equation of motion for  $N$  leads to

$$S(\omega_s, T) = -2\text{Im}[\mathcal{E}^*(\omega_s - \omega_0) \int dt e^{i\omega_s(t-T)} \langle \mu(t) \rangle \cdot e] \quad (6)$$

Expanding the evolution of the dipole operator  $\langle \mu(t) \rangle$  to first order in  $\mathcal{E}$  gives:

$$S(\omega_s, T) = -2\text{Im}[\mathcal{E}^*(\omega_s - \omega_0) \int dt \int_0^\infty dt_1 \mathcal{E}(t - t_1 - T) e^{i(\omega_s - \omega_0)(t - t_1 - T)} e^{i\omega_s t_1} \times i \langle \Psi(t) | \mu \cdot \mathbf{e} G_0(t, t - t_1) \mu^\dagger \cdot \mathbf{e} | \Psi(t - t_1) \rangle] \quad (7)$$

Here,  $|\Psi(t)\rangle$  represents the free evolution of the system following the pump pulse. This is expanded on the basis  $|\phi_e\rangle$  of adiabatic electronic states

$$|\Psi(t)\rangle = \sum_e c_e(t) |\chi_e(t)\rangle |\phi_e\rangle \quad (8)$$

where  $|\chi_e(t)\rangle$  is the time-dependent normalized nuclear wave packet on the  $e$ th valence-state potential energy surface and  $c_e(t)$  is the amplitude of the  $e$ th state. The operator

$$G_0(t, t - t_1) = \sum_f G_{0,ff}(t, t - t_1) |\phi_f\rangle \langle \phi_f| \quad (9)$$

represents the free evolution of the molecule after it has been excited to a core state  $f$ , where  $G_{0,ff}(t, t - t_1)$  is an operator in the nuclear space. By expanding the signal on the basis of adiabatic electronic states, we obtain:

$$S(\omega_s, T) = -2\text{Im}[\mathcal{E}^*(\omega_s - \omega_0) \int dt \int_0^\infty dt_1 \mathcal{E}(t - t_1 - T) e^{i(\omega_s - \omega_0)(t - t_1 - T)} e^{i\omega_s t_1} \sum_{ee'f} c_{e'}^*(t) c_e(t - t_1) \langle \chi_{e'}(t) | \mu_{e'f} \cdot \mathbf{e} G_{0,ff}(t, t - t_1) \mu_{fe}^\dagger \cdot \mathbf{e} | \chi_e(t - t_1) \rangle] \quad (10)$$

Since the core state is short-lived, we neglect the propagation of the nuclear WP on the core state potential energy surfaces and describe it as the electronic modulation in core state  $f$  during  $t_1$ ,

$$G_{0,ff}(t, t - t_1) = e^{-i\omega_f t_1 - \Gamma_f t_1} \quad (11)$$

We have used the following lifetime broadenings 0.613 eV (S 1s-edge), 0.18 eV (O 1s-edge), and 0.132 eV (N 1s-edge).<sup>27</sup> The signal finally reads

$$S(\omega_s, T) = 2\text{Re}[\mathcal{E}^*(\omega_s - \omega_0) \int dt \int_0^\infty dt_1 \mathcal{E}(t - t_1 - T) e^{i(\omega_s - \omega_0)(t - T)} e^{i(\omega_0 - \omega_f + i\Gamma_f)t_1} \times \sum_{ee'f} c_{e'}^*(t) c_e(t - t_1) \langle \chi_{e'}(t) | \mu_{e'f} \cdot \mathbf{e} \mu_{fe}^\dagger \cdot \mathbf{e} | \chi_e(t - t_1) \rangle] \quad (12)$$

The optical pump-X-ray probe signal for a single broadband probe reads

$$S(\omega_s, T) = 2\text{Re}[\mathcal{E}_{\text{pr}}^*(\omega_s - \omega_{\text{pr}}) \int dt \int_0^\infty dt_1 \mathcal{E}_{\text{pr}}(t - t_1 - T) e^{i(\omega_s - \omega_{\text{pr}})(t - T)} e^{i(\omega_{\text{pr}} - \omega_f + i\Gamma_f)t_1} \times \sum_{ee'f} c_{e'}^*(t) c_e(t - t_1) \langle \chi_{e'}(t) | \mu_{e'f} \cdot \mathbf{e} \mu_{fe}^\dagger \cdot \mathbf{e} | \chi_e(t - t_1) \rangle] \quad (13)$$

Replacing the single broadband probe pulse with a broadband/narrowband hybrid pulse,  $\mathcal{E}_B/\mathcal{E}_N$  gives

$$S(\omega_s, T) = 2\text{Re}[\mathcal{E}_B^*(\omega_s - \omega_B) \int dt \int_0^\infty dt_1 \mathcal{E}_N(t - t_1 - T) e^{i(\omega_s - \omega_N)(t - T)} e^{i(\omega_N - \omega_f + i\Gamma_f)t_1} \times \sum_{ee'f} c_{e'}^*(t) c_e(t - t_1) \langle \chi_{e'}(t) | \mu_{e'f} \cdot \mathbf{e} \mu_{fe}^\dagger \cdot \mathbf{e} | \chi_e(t - t_1) \rangle] \quad (14)$$

where  $\omega_N$  is the central frequency of the narrowband field giving the resonance conditions:  $\omega_N = \omega_f$ .

The simulation of TRXAS signal with optical pump and resonant X-ray probe using eqs 13 and 14 requires the following quantities:

- the electronic structure of the valence manifold  $|\epsilon\rangle$  accessible by the optical pump pulse
- the evolution of the system in the valence manifold including phenomena such as IC or ISC
- the electronic structure of the core-excited manifold resonant with the X-ray probe
- the transition dipole moments between the valence and core-excited manifolds

In the following, we have performed pump-probe spectroscopy simulations to track the ultrafast  $\pi\pi^* \rightarrow n\pi^*$  IC process in 4TU. The necessary ingredients are obtained at the ab initio level by combining state-of-the-art multiconfigurational wave function-based electronic structure calculations with grid-based exact quantum dynamics in reduced two-coordinate space.

**Electronic Structure Calculations.** The electronic structure of the valence manifold was obtained at the state-average complete active space self-consistent field (CASSCF) level followed by the single state (SS) flavor second-order perturbation (CASPT2).<sup>29</sup> The active space consists of 12 electrons in 9 orbitals, comprising valence  $\pi$ -orbitals and the sulfur lone pair. Three states, the ground state,  $S_1$  and  $S_2$ , were included in the state averaging. In the CASPT2 routine, an imaginary shift of 0.2 was used,<sup>30</sup> while the IPEA shift was set to 0.0.<sup>31</sup> The ANO-L<sup>32</sup> basis set was used with 5s4p2d1f contractions on sulfur, 4s3p2d1f on carbon, oxygen, nitrogen atoms, and 3s2p1d on hydrogen atoms. Stationary points on the  $S_2$  and  $S_1$  potential energy surfaces (PESs), i.e., the  $S_2$  and  $S_1$  minima and the  $S_2/S_1$  CoIn, were optimized at the SS-CASPT2/SA-3-CASSCF(12,9) level using numerical energy gradients. The ground-state minimum geometry was optimized at the MP2 level.

We have used a different active space and basis set for computing the spectroscopic signals (the calculation of valence-to-core states). In particular, we augment the 12,9 active space with three pairs of occupied ( $\sigma$ )/virtual ( $\sigma^*$ ) orbitals and a single 1s core orbital for each heteroatom S, O, N<sub>1</sub>, and N<sub>2</sub> (see Scheme 1a for the labels). The additional  $\sigma^*$  orbitals are required to converge the core-excited wavefunction



and have a more complete set of spectral signatures in the regions of the PES where C–S and C–C bonds are significantly elongated. We employ the restricted active space formulation of the CASSCF method, known as RASSCF,<sup>33</sup> and place the 1s core orbital of a single heteroatom in RAS1, all occupied orbitals in RAS2, and all virtual orbitals in RAS3, thereby allowing for one hole from RAS1 and up to four excitations into RAS3. We denote this active space as RAS(20,1,4;1,9,6), where the first three indices specify the number of electrons, the number of holes in RAS1, and the number of excitations in RAS3, respectively, while the last three denote the number of orbitals in the three subspaces.

Core-excited-state calculations were performed within the core-valence separation (CVS) framework through a projection technique known as HEXS (highly excited states)<sup>34</sup> which sets to zero CI coefficients of configuration state functions with maximum occupation from a given subspace, thus effectively projecting them out of the wavefunction. In particular, the lowest core-excited states for each heteroatom can be computed by applying the projection to the RAS1 subspace containing the 1s core orbital. Perturbation corrections were obtained with RASPT2,<sup>35</sup> i.e., second-order perturbative correction on top of a RASSCF wavefunction, thereby using an imaginary value of 0.5 and setting the number of frozen orbitals to zero. Scalar relativistic effects were taken into account via a second-order Douglass–Kroll–Hess Hamiltonian in combination with the ANO-RCC basis set<sup>36,37</sup> with contractions 5s4p2d1f on sulfur; 4s3p2d1f on carbon, oxygen, and nitrogen; and 2s1p on hydrogen. At selected points, initial tests with up to 30 core-excited states were performed that showed that a state averaging of 10 states is sufficient in the case of oxygen and nitrogen to capture the dominant absorption signatures below the K-edge, whereas 30 states were averaged in the case of sulfur. A thorough benchmarking of the protocol has demonstrated a sub-eV accuracy of the predicted transition energies.<sup>38</sup> The valence states, ground state,  $S_1$ , and  $S_2$ , were recomputed with the same protocol, i.e., with the 1s core orbital in RAS1, thereby deactivating the projection technique. This allows us to compute transition dipole moments (TDM) between valence and core-excited states via the RASSI module in OpenMolcas.<sup>34</sup>

All quantum chemical calculations were performed with OpenMolcas<sup>39</sup> using the COBRAMM.<sup>40</sup> The core-excited calculations were performed on around 100 geometries constituting the two-dimensional grid used to perform the quantum dynamics simulations (see the [Wavepacket Simulations](#) section).

Due to the random nature of the definition of the wavefunction phase in quantum chemistry software, properties such as the TDM acquire discontinuities in their profiles when represented on a grid. This can affect the sign of contributions to the overall signal due to the loop diagrams ([Scheme 1b](#)), where state indices  $e$  and  $e'$  differ. A wavefunction phase tracking protocol was therefore implemented to obtain continuous TDM profiles. In the following, we outline the procedure on the example of a state  $i$  from the manifold of valence states  $e$  (i.e.,  $e_i$ ) and state  $a$  from the manifold of core-excited states  $f$  (i.e.,  $f_a$ ). At a reference geometry  $k$  (chosen at one of the grid's edges), the sign of the TDM  $\langle e_i^k | r^k | f_a^k \rangle$  is established. Subsequently:

- (a) the overlap matrix between valence states ( $\langle e^k | e^{k'} \rangle$ , dimensions  $3 \times 3$ ) and between core-excited states

( $\langle f^k | f^{k'} \rangle$ , dimensions  $30 \times 30$ ) at the reference geometry  $k$  and at an adjacent point  $k'$  is computed;

- (b) state assignment at adjacent point  $k'$  is determined by means of maximum overlap;
- (c) based on the signs of the maximum valence/valence  $\langle e_i^k | e_j^{k'} \rangle$  and core-excited/core-excited  $\langle f_a^k | f_b^{k'} \rangle$  overlaps at the two adjacent points, it is decided whether to retain or invert the sign of the TDM at geometry  $k'$ ; specifically, the sign is changed if only one of the overlaps is negative.

Next, geometry  $k'$  becomes the new reference geometry and steps (a)–(c) are repeated with the next point on the grid, while maintaining wavefunction sign bookkeeping.

**Wavepacket Simulations.** The geometries of the Franck–Condon (FC) point, of the  $S_2$  minimum ( $S_2$  min), and of the  $S_2/S_1$  conical intersection (CoIn) were used to construct two nuclear degrees of freedom for our effective Hamiltonian.<sup>41</sup> The first coordinate  $\nu_{\text{FC} \rightarrow \text{CoIn}}$  is the normalized displacement vector that points from the FC to the CoIn.  $\nu_{\text{FC} \rightarrow S_2 \text{ min}}$  is the displacement vector from the FC to the local  $S_2$  min, which is then orthonormalized with respect to  $\nu_{\text{FC} \rightarrow \text{CoIn}}$ .

All quantities, including the potential surfaces of the electronic states, nonadiabatic coupling between valence states, and transition dipole moments between valence and core-excited states were evaluated at around 100 nuclear grid points where the nuclear WP is energetically accessible. To accurately describe the nonadiabatic couplings near the CoIn area, we have used denser  $26 \times 20$  grid points, spanning 0.5–1.0 Å for  $\nu_{\text{FC} \rightarrow \text{CoIn}}$  and  $-0.15$ – $0.15$  Å for  $\nu_{\text{FC} \rightarrow S_2 \text{ min}}$  reactive coordinates. The spiky nature of nonadiabatic coupling due to phase change across the CoIn is observed in [Figure S1](#). Then, all quantities are discretized on spatial  $128 \times 128$  grid points in  $\nu_{\text{FC} \rightarrow \text{CoIn}}$  and  $\nu_{\text{FC} \rightarrow S_2 \text{ min}}$  by inter/extrapolation.

The nuclear dynamics are launched using a 20 fs full width at half-maximum (FWHM) Gaussian laser pump in resonance with the  $S_0 \rightarrow S_2$  transition as was done experimentally,<sup>9</sup>

$$\mathbf{E}(t) = A_2 e^{-(t-t_0)^2/2\sigma^2} \cos(\omega_{\text{pu}}(t - t_0)) \quad (15)$$

where  $A_2 = 1.0 \times 10^{-2}$  au is the electric field amplitude, giving the total intensity of  $3.509 \times 10^{12}$  W/cm<sup>2</sup>, below the ionization limit.  $\omega_{\text{pu}} = 3.89$  eV is the central frequency corresponding to the energy gap between the ground state and the  $S_2$  state at the FC point, and  $\sigma = 20$  fs is the temporal duration of the pump pulse. We used this intense pump field to obtain a considerable population in the  $S_2$ . Qualitatively, we expect that the path of the nuclear wavepacket (WP) in the excited/ground state will not change substantially upon the decreasing pump intensity, even in the weak field limit. The nuclear WP is then propagated by numerically solving the time-dependent Schrodinger equation on the two-dimensional nuclear grid<sup>42</sup>

$$i\hbar \frac{\partial}{\partial t} \psi = \mathbf{H}\psi = [\mathbf{T}_\nu + \mathbf{V} - \boldsymbol{\mu}\mathbf{E}(t)]\psi \quad (16)$$

where  $\mathbf{T}_\nu$  is the kinetic energy operator of the nuclei in internal coordinates  $\nu$ ,  $\mathbf{V}$  is the potential energy operator, and  $\boldsymbol{\mu}\mathbf{E}(t)$  describes the light–matter interaction.

The Chebychev propagation<sup>42</sup> with a 0.048 fs time step is employed to propagate this wavepacket until the final time of 242 fs. The G-matrix formalism<sup>43</sup> was employed to set up the kinetic energy operator



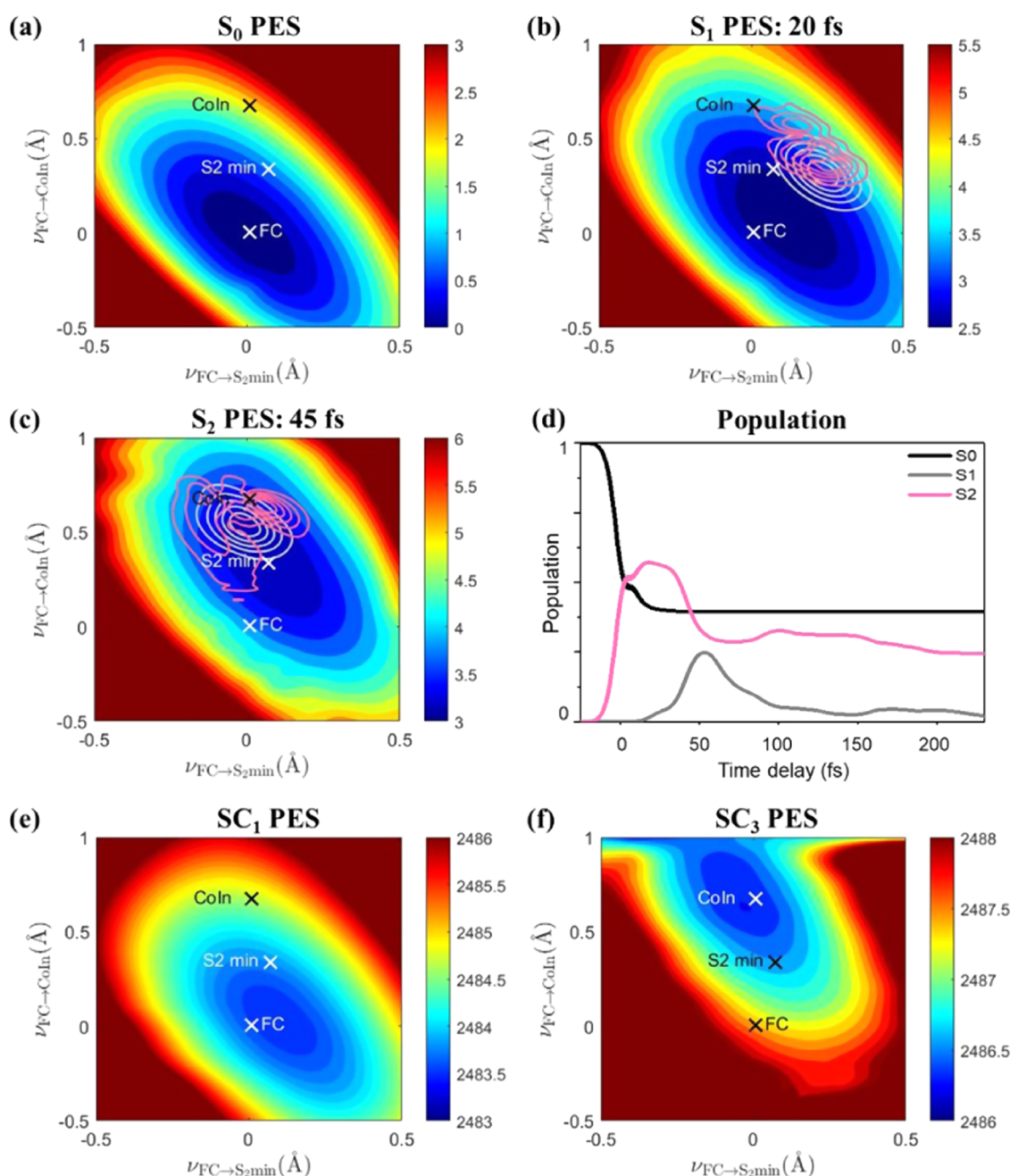


**Figure 1.** Potential energy surfaces and nuclear wavepacket dynamics: (a)  $S_0$  PES, (b)  $S_1$  PES with nuclear wavepacket at 20 fs,  $S_2$  PES with the nuclear wavepacket at 45 fs, (d) state populations, (e)  $SC_1$  PES, and (f)  $SC_3$  PES.  $T = 0$  is set to the maximum intensity of the 20 fs FWHM Gaussian pump.  $S_2$  wavepacket (gray contours),  $S_1$  wavepacket (pink contour). The  $SC_1$  and  $SC_3$  PES refer to the S K-edge core-excited states, which will be discussed in the main text. A movie including  $S_0$ ,  $S_1$ , and  $S_2$  PESs can be found in Figure S3.

$$T_\nu \approx -\frac{\hbar^2}{2m} \sum_{r=1}^M \sum_{s=1}^M \frac{\partial}{\partial \nu_r} [G_{rs} \frac{\partial}{\partial \nu_s}] \quad (17)$$

with the  $G$ -matrix computed via its inverse elements

$$(G^{-1})_{rs} = \sum_{i=1}^{3N} m_i \frac{\partial \mathbf{x}_i}{\partial \nu_r} \frac{\partial \mathbf{x}_i}{\partial \nu_s} \quad (18)$$

For the 4TU coordinates, the  $G$ -matrix elements are  $G_{\nu_r \nu_r} = 0.00007234$  au,  $G_{\nu_s \nu_s} = 0.00009237$  au, and the kinetic coupling  $G_{\nu_r \nu_s} = -0.00002765$  au.

Our effective Hamiltonian was designed for describing the transition from the  $S_2$  to the  $S_1$  state, and it may not accurately

describe the WP propagation in  $S_1$  since other nuclear degrees of freedom not included in our Hamiltonian become relevant. For example, in the vicinity of the  $S_1$  minimum ( $S_1$  min), the  $T_{1/2}$  states are nearly isoenergetic. The wavepacket undergoes ISC, facilitated by a spin–orbit coupling. However, the population of the triplet manifold from the  $S_2$  or  $S_1$  state cannot be described by our two-dimensional Hamiltonian since spin–orbit crossings are not readily accessible by the numerical protocol and the ISC may be facilitated along other modes. Hence, the ISC dynamics is described phenomenologically by absorbing the nuclear wavepacket at the  $S_1$  min with a Butterworth filter operation<sup>44</sup> to prevent major artificial

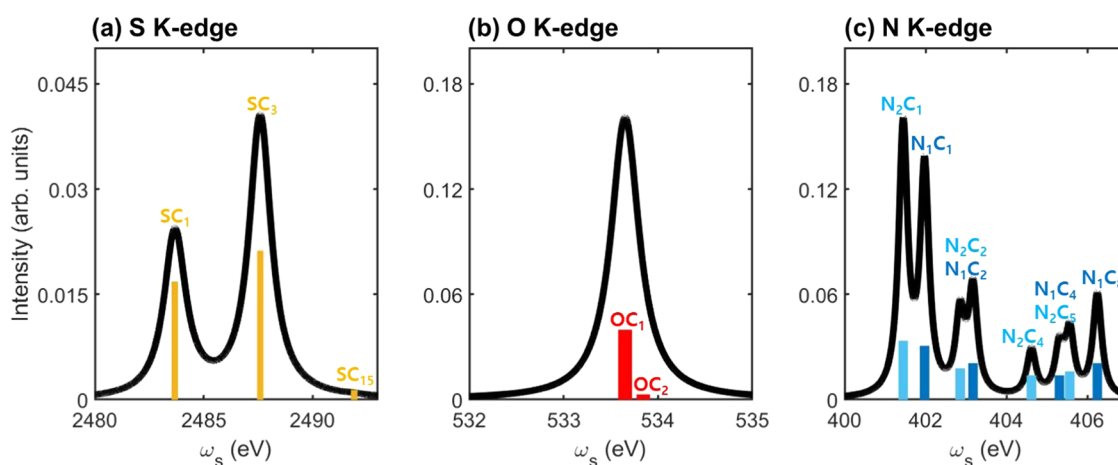


**Figure 2.** Near-edge X-ray absorption fine structure (linear ground-state X-ray absorption spectra) at (a) sulfur, (b) oxygen, and (c) nitrogen K-edges.

back-evolution to  $S_2$ . The filter was of right-pass type and placed at  $\nu_{FC \rightarrow CoIn} = -0.15$  au with an order of 100.

We note that the same valence PES and nonadiabatic couplings were used in our previous study, which focused on off-resonant spectroscopy simulations.<sup>26</sup> In an effort to render the simulations more realistic, here, we use a realistic optical pump to initiate the dynamics. In the previous work, the excited-state wave packet was assumed to be created impulsively.

## RESULTS AND DISCUSSION

First, we briefly describe the photoinduced  $S_2 \rightarrow S_1$  IC dynamics. We simulate with reduced-dimensional nuclear quantum dynamics on a numerical grid spanned by the two reactive coordinates  $\nu_{FC \rightarrow CoIn}$  and  $\nu_{FC \rightarrow S_2 \min}$  describing the motion from the FC to the CoIn and to the  $S_2$  min, respectively. The PESs of the relevant electronic states are displayed in Figure 1a–c. The  $S_2$  PES exhibits a single well with a barrierless pathway from the FC to the  $S_2$  min, which is characterized by pronounced  $C_2C_3$  and  $C_4S$  elongation. Toward the CoIn which lies 0.3 eV above the  $S_2$  min and is nearly isoenergetic with the FC point, the  $C_2-C_3$  is further elongated, in addition to planarity-conserving in-plane bending deformations of oxygen and vicinal hydrogens.

First, an optical UV pump pulse creates a population in the  $S_2$  state. The WP starts from the FC region, then reaches the  $S_2$  min in 20 fs (Figure 1b) and the CoIn in 45 fs (Figure 1c), resulting in relaxation to the  $S_1$  and therefore simultaneous population of both electronic states, termed vibronic coherence. The  $S_2$  WP evolves back to the FC region and oscillates between the FC and the CoIn with a 70 fs period. Both coordinates cooperatively deform the geometry of the molecule leading the nuclear WP from the FC region to the CoIn. The second coordinate,  $\nu_{FC \rightarrow S_2 \min}$  mainly facilitates decoherence between the excited-state nuclear WPs due to the different energy gradient in both states. The  $S_1$  and  $S_2$  WP evolve differently after they arrive at the FC region, and their overlap decreases over time (Figure S3). Surface hopping simulations<sup>9</sup> had reported characteristic C–S stretching (457  $\text{cm}^{-1}$ ) and ring breathing (697 and 783  $\text{cm}^{-1}$ ) modes associated with the dynamics on  $S_2$ . The 70 fs ( $\sim 476 \text{ cm}^{-1}$ ) WP oscillation period in the QD simulations matches nicely the C–S stretching mode period, thereby demonstrating that

the reduced vectors encompass projections on the modes relevant to the dynamics in  $S_2$ . The  $S_1$  WP moves away from the CoIn to the  $S_1$  min, where the ISC mostly takes place. To mimic the ISC process, we absorb the parts of the nuclear WP that reach the  $S_1$  min.

The  $S_2$  population decay (Figure 1d) was fitted with  $P(t) = A e^{-t/k} + P_0$ , where  $P_0 + A$  is the initial population, yielding a time constant  $k$  of 52.4 fs, in agreement with our previous work (56 fs),<sup>26</sup> experiment (76 fs), and surface hopping simulations (67.5 fs).<sup>9</sup>

Before presenting the TRXAS signal, we discuss the core-excited electronic structure of 4TU for the various core atoms. Figure 2 shows the K-edges of sulfur, oxygen, and nitrogen that can be obtained experimentally by near-edge X-ray absorption fine structure (NEXAFS) spectroscopy, a form of linear absorption spectroscopy. We recognize a fine pre-edge structure due to bright core-electron transitions to valence orbitals. Table 1 lists the energies, TDMs, and orbitals involved in the said transitions. These are labeled  $SC_n$ ,  $OC_n$ ,  $N_1C_n$ , and  $N_2C_n$ , where  $n$  is ordered by increasing core state energies at the FC geometry, i.e.,  $SC_1$  indicates the lowest sulfur 1s core-excited state.

The sulfur K-edge exhibits two peaks, at 2483.5 ( $SC_1$ ) and 2487.5 eV ( $SC_3$ ) (Figure 2a), associated with transitions from the 1s core orbital of sulfur into the vacant lowest unoccupied molecular orbital (LUMO)  $\pi_1^*$  and into a  $\sigma_2^*$  orbital, respectively (depicted in Figure 3a). These two orbitals have pronounced MO coefficients on the sulfur, in particular  $\sigma_2^*$  is the antibonding C–S orbital. This highlights an important requirement for core transitions to be optically bright, namely, that the arrival valence orbital must have a non-negligible contribution from basis functions on the atom hosting the 1s core-orbital (highlighted by dashed cyan circles in Figure 3). In agreement with this requirement, the only bright transition in the K-edge of oxygen at 533.5 eV ( $OC_1$ ) is associated with orbital  $\pi_2^*$  (depicted in Figure 3b), while the transition to the LUMO, having no MO coefficient on the oxygen, is dark. We note that also orbital  $\pi_3^*$  (see Figure S2 in the SI) shows a contribution to the oxygen giving rise to a weak band at 533.8 eV ( $OC_2$ , Figure 2b). The nitrogen K-edge is very rich with multiple peaks in the window 401.5–406.5 eV (Figure 2c), which is rationalized not only by the presence of two nitrogen atoms in 4TU but also by their contribution to orbitals  $\pi\pi_{1-3}^*$  (depicted in Figure 3c).

**Table 1. Transition Energies (eV) and Dipole Moments (au) between Valence (Labeled  $S_0$ ,  $S_1$ , and  $S_2$ ) and Core-Excited States (Labeled  $X_{(n)}$ ,  $C_n$  for Sulfur, Oxygen, and Both Nitrogen Atoms of 4TU at the FC Point Geometry)<sup>a</sup>**

valence state	K-edge	root	$\Delta E$ (eV)	$ \mu $ (au)	CSF (weight)
$S_0$	N1	$N_1C_1$	401.98	0.0307	$1s^{[1]}\pi_1^{*[1]}$ (75%)
$S_0$	N1	$N_1C_2$	403.17	0.0208	$1s^{[1]}\pi_2^{*[1]}$ (69%)
$S_0$	N1	$N_1C_4$	405.31	0.0139	$1s^{[1]}\pi_3^{[1]}\pi_1^{*[2]}$ (61%)
$S_0$	N1	$N_1C_8$	406.25	0.0208	$1s^{[1]}\pi_3^{[1]}\pi_1^{*[1]}$ (41%)
$S_0$	N2	$N_2C_1$	401.45	0.0335	$1s^{[1]}\pi_3^{*[1]}$ (77%)
$S_0$	N2	$N_2C_2$	402.86	0.0179	$1s^{[1]}\pi_3^{*[1]}$ (69%)
$S_0$	N2	$N_2C_4$	404.62	0.0139	$1s^{[1]}\pi_3^{[1]}\pi_1^{*[2]}$ (56%)
$S_0$	N2	$N_2C_5$	405.57	0.0162	$1s^{[1]}\pi_3^{[1]}\pi_1^{*[1]}\pi_2^{*[1]}$ (38%)
					$1s^{[1]}\sigma_1^{*[1]}$ (23%)
$S_0$	O	$OC_1$	533.65	0.0399	$1s^{[1]}\pi_2^{*[1]}$ (68%)
$S_0$	S	$SC_1$	2483.68	0.0168	$1s^{[1]}\pi_3^{*[1]}$ (90 %)
$S_0$	S	$SC_3$	2487.60	0.0212	$1s^{[1]}\sigma_2^{*[1]}$ (81 %)
$S_1$ ( $n\pi^*$ )	N1	$N_1C_3$	401.67	0.0249	$1s^{[1]}\pi_1^{[1]}\pi_1^{*[2]}$ (85%)
$S_1$ ( $n\pi^*$ )	N1	$N_1C_5$	402.74	0.0191	$1s^{[1]}\pi_1^{[1]}\pi_1^{*[1]}\pi_2^{*[1]}$ (91%)
$S_1$ ( $n\pi^*$ )	N2	$N_2C_1$	398.50	0.0090	$1s^{[1]}\pi_1^{*[1]}$ (77%)
$S_1$ ( $n\pi^*$ )	N2	$N_2C_3$	401.82	0.0242	$1s^{[1]}\pi_1^{[1]}\pi_1^{*[2]}$ (89%)
$S_1$ ( $n\pi^*$ )	N2	$N_2C_6$	402.96	0.0208	$1s^{[1]}\pi_1^{[1]}\pi_1^{*[1]}\pi_2^{*[1]}$ (90%)
$S_1$ ( $n\pi^*$ )	O	$OC_5$	533.70	0.0393	$1s^{[1]}\pi_1^{[1]}\pi_1^{*[1]}\pi_2^{*[1]}$ (55%)
$S_1$ ( $n\pi^*$ )	S	$SC_1$	2480.73	0.0235	$1s^{[1]}\pi_1^{*[1]}$ (90 %)
$S_1$ ( $n\pi^*$ )	S	$SC_{13}$	2489.14	0.0172	$1s^{[1]}\pi_1^{[1]}\sigma_2^{*[1]}\pi_1^{*[1]}$ (62 %)
$S_2$ ( $\pi\pi^*$ )	N1	$N_1C_1$	397.76	0.0191	$1s^{[1]}\pi_1^{*[1]}$ (75%)
$S_2$ ( $\pi\pi^*$ )	N1	$N_1C_4$	401.09	0.0279	$1s^{[1]}\pi_3^{[1]}\pi_1^{*[2]}$ (61%)
$S_2$ ( $\pi\pi^*$ )	N1	$N_1C_8$	402.03	0.0110	$1s^{[1]}\pi_3^{*[1]}$ (41%)
$S_2$ ( $\pi\pi^*$ )	N1	$N_1C_9$	402.59	0.0069	$1s^{[1]}\pi_3^{[1]}\pi_1^{*[1]}\pi_2^{*[1]}$ (30%)
$S_2$ ( $\pi\pi^*$ )	N2	$N_2C_1$	397.23	0.0226	$1s^{[1]}\pi_3^{*[1]}$ (77%)
$S_2$ ( $\pi\pi^*$ )	N2	$N_2C_4$	400.40	0.0249	$1s^{[1]}\pi_3^{[1]}\pi_1^{*[2]}$ (56%)
$S_2$ ( $\pi\pi^*$ )	O	$OC_8$	533.62	0.0376	$1s^{[1]}\pi_3^{[1]}\pi_1^{*[1]}\pi_2^{*[1]}$ (45%)
$S_2$ ( $\pi\pi^*$ )	S	$SC_1$	2479.46	0.0157	$1s^{[1]}\pi_1^{*[1]}$ (90%)
$S_2$ ( $\pi\pi^*$ )	S	$SC_3$	2483.38	0.0099	$1s^{[1]}\sigma_2^{*[1]}$ (81%)
$S_2$ ( $\pi\pi^*$ )	S	$SC_{15}$	2487.70	0.0155	$1s^{[1]}\pi_3^{[1]}\sigma_2^{*[1]}\pi_1^{*[1]}$ (37%)

<sup>a</sup>Leading configuration state functions (CFS) and corresponding weights are also shown.

The valence  $\pi\pi^*$  and  $n\pi^*$  states exhibit semivacant occupied orbitals labeled  $\pi_5$  MO and  $n$  (Figure 3) that can act as arrival orbitals for the core-excited electrons, giving rise to additional signals in the transient X-ray spectra. Moreover, as occupied valence orbitals are energetically more stable than virtual ones, the transient signals are expected to be red-shifted by several eV in a background-free pre-edge region, making them particularly appealing for studying electronic states (ES) dynamics. As an example, the sulfur  $1s \rightarrow n$  transition from the  $n\pi^*$  state and the  $1s \rightarrow \pi_5$  transition from the  $\pi\pi^*$  state appear at 2480.5 ( $n\pi^* \rightarrow SC_1$ ) and 2479.5 eV ( $\pi\pi^* \rightarrow SC_1$ ), respectively, i.e., 3–4 eV below the lowest ground-state absorption feature. In the nitrogen K-edge, the  $1s \rightarrow n$  transition from  $N_2$  (i.e., the nitrogen next to the thiocarbonyl group) is weakly dipole-allowed since the lone pair is partially delocalized over the vicinal atoms. The corresponding transition from  $N_1$  is completely dark.

Further transitions into virtual orbitals, such as the sulfur  $1s \rightarrow \sigma_2^*$  or nitrogen  $1s \rightarrow \pi_1^*$ , which could be also probed from the valence excited states, are expected to overlap with the corresponding absorption features from the ground state, giving rise to a complex pattern. For example, we had already established the  $1s \rightarrow \pi_2^*$  transition is the only bright transition in the K-edge of oxygen. This transition can also be excited from the  $n\pi^*$  and  $\pi\pi^*$  state, giving rise to doubly excited hybrid states  $OC_5$  and  $OC_8$  with configurations  $1s^{[1]}\pi_1^{[1]}\pi_1^{*[1]}\pi_2^{*[2]}$  and  $1s^{[1]}\pi_3^{[1]}\pi_1^{*[1]}\pi_2^{*[2]}$  absorbing around 533.5 eV, thereby matching the energy of the  $1s \rightarrow \pi_2^*$  from the ground state. We thus expect that transient and ground-state absorption contribution should largely cancel out for K-edges of atoms not involved in the IC. On a side note, the presence of intense contributions in the transient spectra from doubly excited electronic states highlights the necessity to use multiconfigurational methods, capable of treating single and double excitations at equal footing, for a complete description of the K-edge in the simulations. In density functional theory, these hybrid states are not straightforwardly accessible but can be described to some extent by coupling core-excited electronic structure calculations to the maximum overlap method, which provides access to excited state self-consistent field solutions.<sup>25,45</sup>

Next, we present the optical pump-resonant X-ray probe TRXAS signals represented by the loop diagram given in Scheme 1b from an ensemble of randomly oriented molecules. We use a single broadband probe pulse (Scheme 1, 15 eV bandwidth) and tune its central frequency to the sulfur (2483.5 eV), oxygen (533.5 eV), and nitrogen (402 eV) K-edges. The signals were computed using eq 13 in the  $x$ ,  $y$ , and  $z$  polarization direction in the molecular frame and then rotationally averaged with a second rank tensor, leading to

$$\langle S(\omega_s, T) \rangle_\Omega = \frac{1}{3} [S_{xx}(\omega_s, T) + S_{yy}(\omega_s, T) + S_{zz}(\omega_s, T)] \quad (19)$$

where  $S_{xx/yy/zz}$  represents the optical pump-resonant X-ray probe signal calculated with  $x/y/z$  components of transition dipoles (i.e.,  $\mu_{e'fx}$  and  $\mu_{fe,x}^\dagger$ ), respectively.

The signals calculated at the three K-edges are displayed in Figure 4a–c top left panel, respectively, showing positive (red) and negative (blue) contributions. In agreement with the preceding discussion, the negative peaks arise from the ground-state absorption to  $SC_1$  (2483.7 eV),  $SC_3$  (2487.5 eV) for sulfur K-edge,  $OC_1$  (at 533.5 eV) for oxygen K-edge, etc. (also known as ground state bleach, GSB) and constitute a steady background. Positive contributions arise due to photoinduced absorption (PA) from transiently populated valence excited states, which exhibit rise and decay in response to the electronic dynamics while simultaneously modulated by oscillatory features due to vibrational dynamics.

Herein, we emphasize that the  $S_2/S_1$  PESs have mainly  $\pi\pi^*/n\pi^*$  electronic character, respectively. Generally, the electronic character switches across the CoIn, e.g.,  $S_2$  PES exhibits the  $\pi\pi^*$  character before crossing the CoIn, but  $n\pi^*$  character thereafter. However, in 4TU, where the electronic energies at the FC and the CoIn are similar, the WP cannot cross over the CoIn area but bounces back to the FC point. The nuclear WP is predominantly propagated before the CoIn at all times, with only very minor parts actually crossing the CoIn. We thus cautiously discuss the photoinduced absorption from the  $S_2$



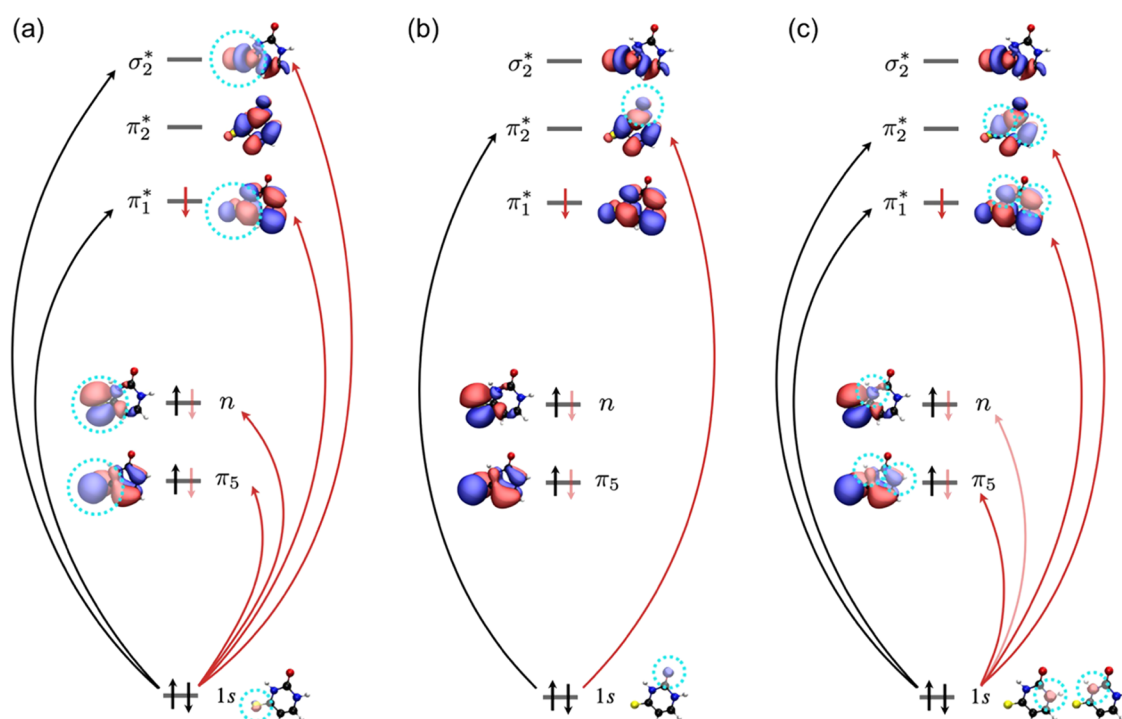


**Figure 3.** Core-to-valence transitions giving rise to features in the near-edge X-ray absorption fine structure (NEXAFS, Figure 2) and optical pump-resonant X-ray probe (TRXAS, Figure 4) spectra at (a) sulfur, (b) oxygen, and (c) nitrogen K-edges. Core and valence orbitals are shown. Black and red lines denote transitions from the electronic ground ( $S_0$ ) and valence excited ( $S_1$  and  $S_2$ ) states, respectively. Dashed cyan circles highlight valence orbitals, the contributions of which are from the heteroatom involved in the core excitation.

and the  $S_1$  using  $\pi\pi^*/n\pi^*$  nomenclature, even though we did not perform an explicit diabaticization.

The  $SC_1$  signal at 2480 eV is the only core-excited state, which is simultaneously bright from both  $\pi\pi^*$  and  $n\pi^*$  excited states since the relevant transition densities are localized on the sulfur. The signal rises immediately after the  $S_2$  is populated and remains strong even upon CoIn passage as the decrease of  $S_2$  population is compensated by the increase of  $S_1$  population, i.e., the decay of the  $\pi\pi^*$  contribution coincides with the rise of the  $n\pi^*$  absorption (Figure 4a, middle panels). After the CoIn passage, the  $S_2$  and  $S_1$  nuclear WPs propagate in their respective PESs with finite splitting. The spectral trace at 60 fs at the bottom right panel (red lines) exhibits the double-peak structure due to the PA coming from the  $\pi\pi^*$  (gray) and the  $n\pi^*$  (pink). The PA signal splitting clearly shows signatures of the bifurcation of the coherent nuclear WP. The  $SC_3$  and  $SC_{15}$  states are fingerprint PA features of  $\pi\pi^*$ . The  $SC_{13}$  state, in contrast, is dipole-allowed only from  $n\pi^*$ , thus is observable only when the nuclear WP reaches CoIn area (after 45 fs) and the  $S_1$  state, exhibiting  $n\pi^*$  character, has significant populations. Note, however, that the spectral overlap of  $SC_{13}$  and  $SC_{15}$  makes it hard to resolve the  $n\pi^*$  contributions from the  $\pi\pi^*$  ones in the sulfur K-edge.

All PA signals in the sulfur K-edge exhibit quantum beating (i.e., coherent intensity oscillations), intensity oscillation of which depends on the vibrational coordinate, the transfer of population to other states with varying transition dipole moments along the grid, and the different electronic character of the core states. First, the quantum beat originating from the vibration coordinate can be observed from the fact that the intensity oscillation is repeated with the period of 70 fs, corresponding to the C–S stretching mode of our reactive coordinates. The population transfer to the  $S_1$  state, which has

mainly  $n\pi^*$  character, and thus its dark TDM against  $SC_3$  state make the quantum beat at 2482.5 eV strong in the beginning (bottom left panel in Figure 4a) when the nuclear WP is localized at the FC point, but weaker after the nuclear WP reaches the CoIn area. In contrast, the quantum beat at 2480.2 eV (transition to  $SC_1$ ) is strongest between 20 and 40 fs, when the nuclear WP passes by the  $S_2$  min and the CoIn area, where the large transition dipole moment between the  $S_1$  and  $SC_1$  state can contribute to the PA. Finally, the  $SC_1$  band differs from the patterns of the  $SC_{3/13/15}$  bands. In particular, we see a redshift of the  $SC_{3/13/15}$  signals during the motion toward the CoIn and a blueshift during the motion away from it. The opposite trend is observed for the  $SC_1$  signal. States  $SC_{3/13/15}$  have in common a transition into the  $\sigma_2^*$  localized on the C–S bond. Due to the antibonding nature of the orbital, the core-excited PES exhibits its minimum at elongated C–S, i.e., in the direction of the CoIn (Figure 1f). Thus, during the motion of the WP toward the CoIn, the valence-to-core-excited energy gap decreases, leading to the observed redshift of the PA. In  $SC_1$  the core electron is brought away from the sulfur into a  $\pi^*$  orbital delocalized over the entire ring, which leads to a decrease in the nuclear charge shielding around the sulfur. This causes the heteroatom to withdraw electron density from the nearby carbon strengthening the bond. As a consequence, the C–S bond shortens at the  $SC_1$  PES minimum (Figure 1e). Thus, during the WP motion toward the CoIn, the valence-to-core-excited energy gap increases, which translates into a blueshift of the PA. Thus, the pump-probe signal provides spectroscopic signatures of the relevant nuclear motion on the PES, which can be extracted by first subtracting the electronic dynamics, itself accessible through global fitting, and subsequently Fourier transforming the residuals.<sup>6,9</sup>

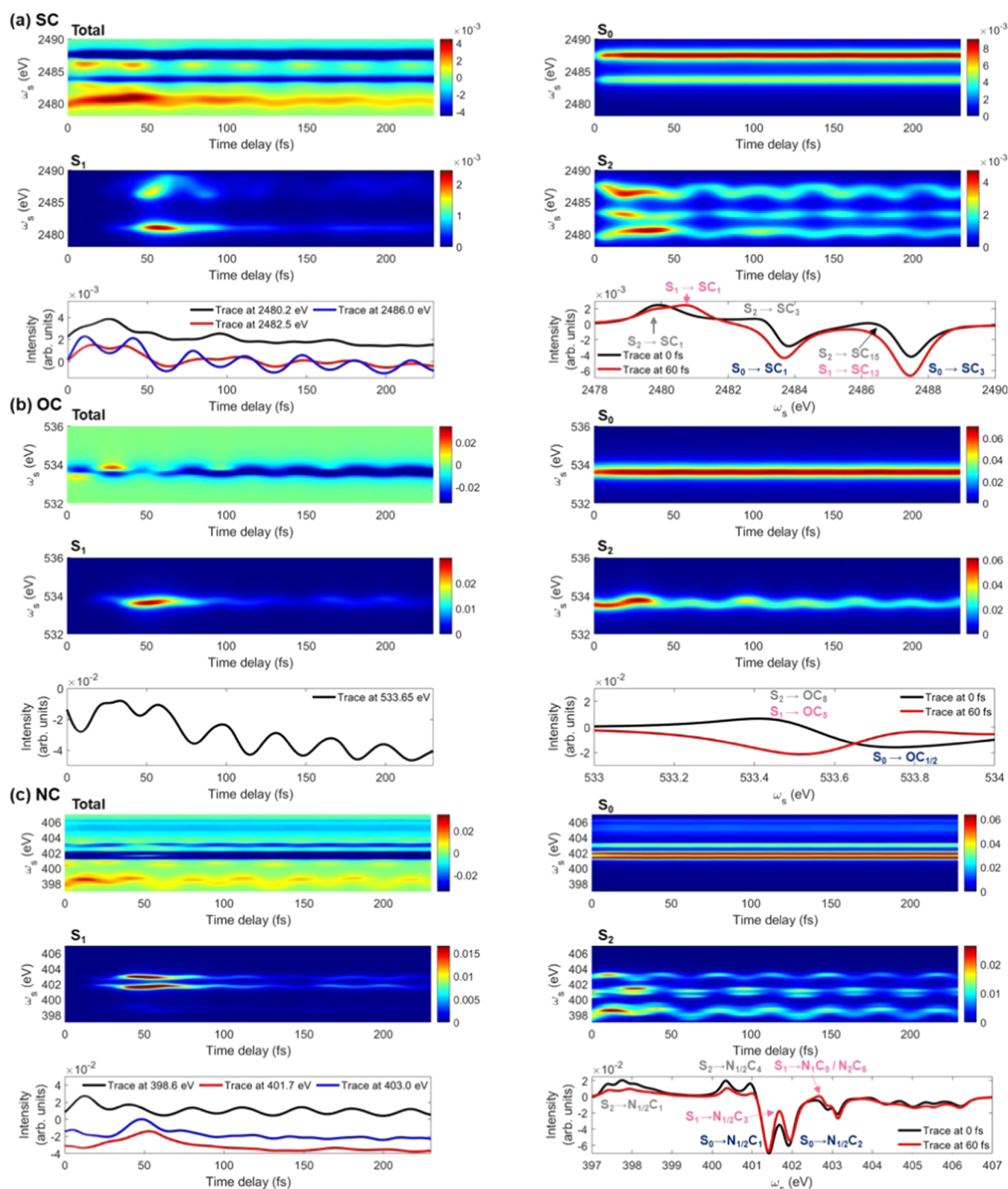


**Figure 4.** Simulated optical pump-X-ray probe signals of 4TU calculated with single broadband probe field at (a) sulfur, (b) oxygen, and (c) nitrogen K-edges. The top and middle panels show the total signal (top left) and the contribution to the total signal from each valence state. The negative contribution to the total signal comes from the ground-state bleach background. The bottom panels show the temporal (left) and spectral (right) trace of the total signal (black, red, and blue) at certain detection frequency and time delay, respectively. The navy, pink, and gray arrows and texts indicate the involved electronic transition from the  $S_0$ ,  $S_1$ , and  $S_2$  valence state to the core manifold, respectively.

As discussed above, for the oxygen K-edge (Figure 4b), the lowest core-excited state is not dipole-allowed from the valence

excited states but accessible from the ground state. Its oscillator strength is too weak to be visible in the spectra

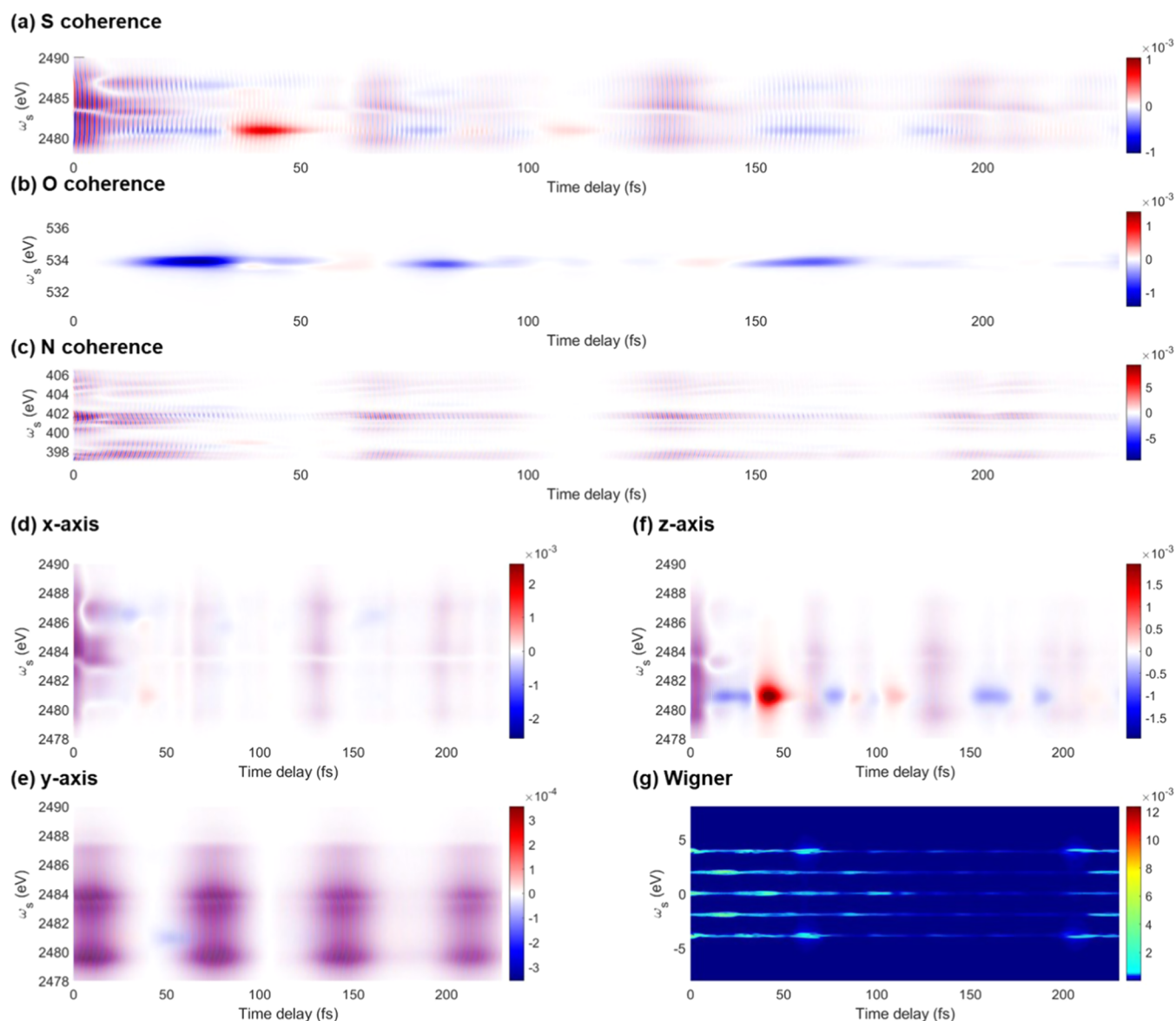


**Figure 5.** Coherence contribution to the total signal at (a) sulfur, (b) oxygen, and (c) nitrogen K-edges. Coherence contribution to the sulfur K-edge signal along (d) *x*-axis (e) *y*-axis, and (f) *z*-axis. (g) Wigner spectrogram integrating the temporal trace  $S(t)$  of the signal over  $\omega_s = 2477.2$ – $2492.4$  eV.

since the oxygen atom only makes a minor contribution to  $\pi_s^*$  and to the sulfur lone pair.  $n\pi^*$  and  $\pi\pi^*$  have one particularly bright core-excited state each, labeled  $OC_5$  and  $OC_8$ , respectively, associated with the  $1s \rightarrow \pi_2^*$  transition, that has a nonvanishing molecular orbital component on the oxygen atom. We note that the GSB and PA largely cancel out as the oxygen is insensitive to the molecular deformation along the 2D grid, confirming our expectation based on the analysis of the FC electronic structure. The valence to core-excited gap remains relatively constant throughout the grid, with a value of ca. 533.5 eV. While not being informative about the IC, it demonstrates how nonreactive groups generate a steady transient PA that shows no spectral dynamics.

For the nitrogen K-edge (Figure 4c), while we are in the position to computationally distinguish core transitions from either  $N_1$  or  $N_2$ , we note that for broadband-probe TRXAS, signals from both atoms will be observed simultaneously. The lowest core states,  $N_1C_1$  and  $N_2C_1$ , are well separated from

higher ones and GSB, yielding the positive PA signatures. They exhibit strong resonances at 398 to 399 eV due to their large transition dipole moments from the  $\pi\pi^*$  state, while the  $n\pi^*$  contribution is weak and negligible. Accordingly, the signal intensities decrease when the nuclear WP passes through the CoIn at 45 fs (bottom left panel in Figure 4c, black line). Hence, the lowest nitrogen core states provide spectral fingerprints for extracting the  $\pi\pi^*$  lifetime. On a side note, we bring to the reader's attention that the intensity decrease of a PA signal is not necessarily the consequence of population transfer to another state as it could be the result of decrease of the TDM along the grid for a given electronic state. To demonstrate this, Figure S5 shows plots of the TDM magnitude along the grid, evidencing that some transitions exhibit multifold variations of the TDM strength (e.g.,  $S_2 \rightarrow N_1C_4$ ) that would translate in fluctuations of the peak intensity even in adiabatic dynamics.



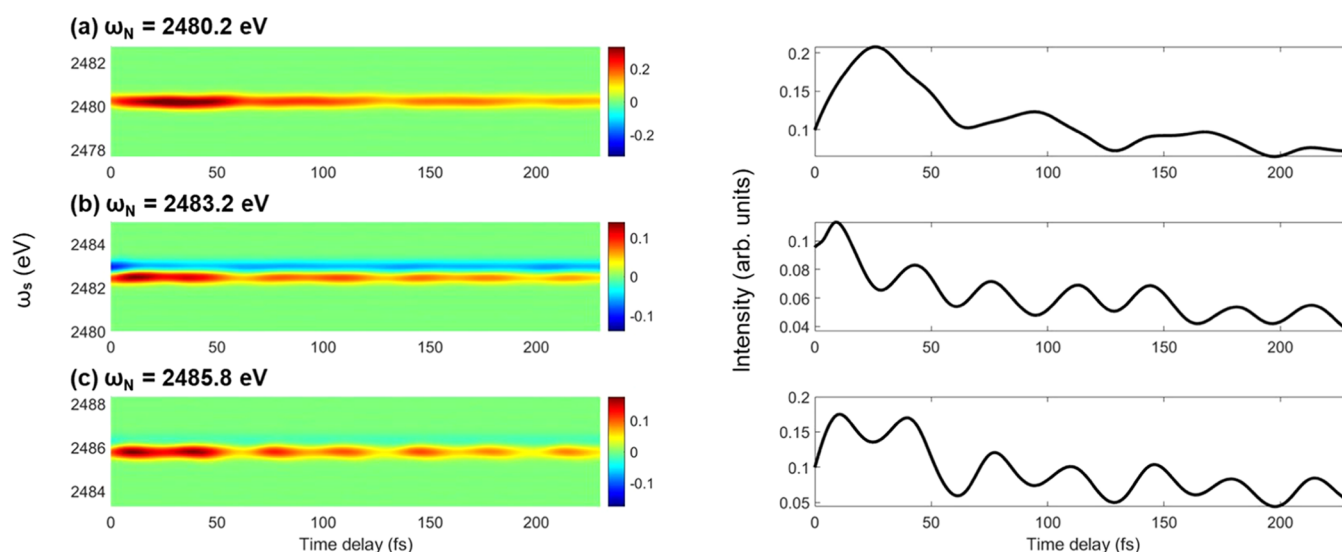


**Figure 6.** Optical pump-resonant X-ray probe signal calculated with hybrid field (left) for S K-edge at  $\omega_N$  = (a) 2480.2 eV, (b) 2483.2 eV, and (c) 2485.8 eV. The temporal trace of the signal calculated with single broadband at the same central frequency is given on the right panels.

PA features from the  $n\pi^*$ , arising at around 401.7 eV ( $N_1C_3$  and  $N_2C_3$ ) and 403.0 eV ( $N_1C_5$  and  $N_2C_6$ ). The  $N_1$  and  $N_2$  absorption lines overlap, giving a distinctive strong absorption line with a delayed rise. By taking the temporal trace at 401.7 and 403.0 eV, marked by red and blue lines at the bottom left panel, one could retrieve the PA signature from the  $n\pi^*$  through the depletion of the GSB. Note that the GSB marks the steady background due to the localized nuclear WP at the  $S_0$  PES.

We would expect to observe PA signatures of the triplet state rising on a several hundred femtosecond time scale following the ISC.<sup>9</sup> Note that, while the triplet state has a characteristic PA in the visible region, the  $n\pi^*$  state is dark and its involvement in the photophysics of 4TU has been inferred only indirectly, based on the mismatch between the decay of the SE from the  $\pi\pi^*$  and the rise of the triplet PA.<sup>9</sup> The TRXAS simulations show that the nitrogen K-edge is well suited to track the population dynamics in both the  $\pi\pi^*$  and  $n\pi^*$  states.

The TRXAS signal involves both excited/ground-state absorption ( $e = e'$ ) and Raman transition components ( $e \neq e'$ ), which are relevant to the electronic coherence. The requirements for strong coherence contributions can be inferred from eq 13: (a) comparable populations in both valence states  $e$  and  $e'$  with overlapping WP; (b) core-excited states that are dipole-allowed simultaneously from both valence states; and (c) parallel or antiparallel orientation of the corresponding TDMs. We found that for the oxygen K-edge (Figure 5b), the  $S_2/S_1$  coherence is extremely weak (3 orders smaller than populations) since each valence state is coupled to a different core-excited state. The sulfur (Figure 5a) and nitrogen K-edge (Figure 5c), in contrast, exhibit contributions from electronic coherences in the spectra, which are only an order of magnitude less intense than contributions from populations as there are core-excited transitions, which are dipole-allowed from more than one state. The  $S_2/S_0$  coherence in sulfur K-edge is observed at 2480, 2483.7, and 2487 eV through the  $SC_1$ ,  $SC_3$ , and  $SC_{15}$  core states, respectively. They are strong at the beginning of the simulation when the  $S_2$  WP is localized at the FC region since the  $S_2/S_0$  overlap is maximal. With the evolution of the

WP away from the FC, the overlap decreases and eventually vanishes completely. To visualize the dynamical evolution of this frequency, we display an integrated Wigner spectrogram of temporal traces  $S(T)$  of the coherence contribution over  $\omega_s = 2477.2$  eV to 2492.4 eV in Figure 5g.

$$W(T, \omega_{\text{coh}}) = \int_{-\infty}^{\infty} d\tau S(T + \tau) S(T - \tau) e^{i\omega_{\text{coh}}\tau} \quad (20)$$

The main feature appears around 4 eV, which coincides with the energy gap between the ground state and the  $S_2$  state. A weak  $S_2/S_1$  coherence contribution is observed at 2481 eV due to the finite TDM between the valence excited states and  $SC_1$  but is masked by the population background, making it hard to extract. The  $SC_1$  state is dipole-allowed from both  $\pi\pi^*$  and  $n\pi^*$ , but actually, the corresponding TDMs along  $y$  and  $z$  axes are orthogonal to each other (see their opposite phase at 2481 eV in Figure 5e,f). Due to the weak excitation by the  $y$ -linearly polarized pump, the  $S_2/S_1$  coherence survives and can be observed. Otherwise, their orthogonality leads to a vanishing coherence intensity after rotational averaging. The  $S_2/S_1$  coherence appears in the Wigner spectrogram at 45 fs at around 0 eV and gives the approximate timing of the  $S_2/S_1$  CoIn passage. A similar argumentation can be applied to nitrogen K-edge.

In the following, we show that the use of a hybrid narrow/broadband field provides a similar information with a narrower detection window, providing a specific single-core-state information. A femtosecond narrowband pulse  $\mathcal{E}_N$  excites a system on a valence electronic state  $|e\rangle$  into a core level  $|f\rangle$ . Then, the attosecond broadband  $\mathcal{E}_B$  stimulates the emission. The inverse setup in which a broadband pulse is used to excite the system into a core level  $|f\rangle$ , whereas stimulated emission is realized by a narrowband pulse gives identical information. In both setups, the detection window is limited by the narrowband, whereas the attosecond broadband pulse proves the temporal resolution. The relevant pulse configuration and loop diagram are shown in Figure S6.

The narrowband pulse  $\omega_N$  with 0.6 eV bandwidth was scanned over the sulfur K-edge between 2475 to 2490 eV to find the resonances. This bandwidth corresponds to the narrowest spectral resolution of XFEL with a central frequency

of 2 keV that can be gained with the current free-electron laser technology to the best of our knowledge. Equation 14 indicates that the detected signal is centered at the narrowband central frequency  $\omega_N$  due to the resonance condition. Otherwise, the term  $e^{i(\omega_N - \omega_j)t_1}$  rapidly oscillates along  $t_1$  which makes the integration over  $t_1$  vanish.

In Figure 6a–c, we represent the signal at  $\omega_N = 2480.2$ , 2483.2, and 2485.8 eV associated with transitions to  $SC_1$ ,  $SC_3$ , and  $SC_{13/15}$ . One can selectively probe the time-evolving spectral signature of a core-to-valence transition at a given detection frequency. Using a broader incoming X-ray pulse (e.g., 4 eV) would allow us to monitor time-evolving absorption lines of several core states (e.g.,  $SC_1$  and  $SC_3$ ) at the same time. We note that simulating the hybrid pulse TRXAS is identical to taking the temporal trace of the TRXAS simulated with a single broadband pulse in a 0.6 eV wide frequency window (compare the left and the right panels in Figure 6). For example, the double-peak nature observed for  $SC_{13/15}$  at 2485.8 eV is well represented in Figure 6c.

## CONCLUSIONS

We have simulated the optical pump-resonant X-ray probe (TRXAS) signals, which monitor the  $\pi\pi^* \rightarrow n\pi^*$  internal conversion process in 4TU. Exact quantum nuclear wavepacket dynamics performed on a two-dimensional PES grid reproduces the relaxation dynamics in good agreement with the experiment. A multiconfigurational wavefunction-based protocol using restricted active space self-consistent field and multireference perturbation theory (RASSCF/RASPT2) allows access to the electronic structure of the core-excited manifold with high accuracy. Treatment of single-core-excited and double-hybrid (core + valence)-excited states on an equal footing assures the completeness of the transient spectra. The high-level electronic structure method reveals the characteristics of 4TU, where the  $S_2/S_1$  PES is dominated by the  $\pi\pi^*/n\pi^*$  electronic character, due to the similar potential energy at the FC and the CoIn.

The simulated signals for various K-edges provide element-specific photoinduced absorption fingerprints of the  $\pi\pi^*$  and  $n\pi^*$  states. The lowest sulfur K-edge shows a strong coherently oscillating resonance, which is dipole-allowed from both  $\pi\pi^*$  and  $n\pi^*$  states in a background-free pre-edge window. The oxygen K-edge is not sensitive to molecular deformations and, as a consequence, exhibits a steady spectrum of strongly overlapping GSB and PA contributions. The lowest nitrogen PA marks the fingerprint of the  $\pi\pi^*$  state, and the decay of its intensity gives an approximate timing for the CoIn passage. Notably, an intense  $n\pi^*$  spectral signature can be observed around 402 to 403 eV, facilitating the direct observation of its delayed population and the timing of the ISC. The  $\pi\pi^*/n\pi^*$  electronic coherence is weak and covered by the much stronger population contributions.

In conclusion, TRXAS provides complementary information to off-resonant techniques such as TRUECARS by resolving the time scale of IC and ISC. The resonant technique is not suitable for resolving coherences built upon CoIn passage, thus emphasizing the need for off-resonantly tuned X-ray pulses to separate electronic coherences from population contributions. Substituting the single attosecond broadband probe pulse into a hybrid narrow/broadband field allows us to probe individual core states separately but does not provide additional insights into the photophysics; thus, its implementation is discouraged.

## ASSOCIATED CONTENT

### Supporting Information

The Supporting Information is available free of charge at <https://pubs.acs.org/doi/10.1021/acs.jctc.2c00064>.

Loop diagram rule, nonadiabatic coupling map, active space, nuclear wavepacket molecular dynamics movie, time-evolving electronic states levels, transition dipole moment maps, pulse configuration, and loop diagram for hybrid X-ray probe pulse (PDF)  
Nuclear wavepacket molecular dynamics (AVI)

## AUTHOR INFORMATION

### Corresponding Authors

**Yeonsig Nam** – Department of Chemistry, University of California, Irvine, California 92697-2025, United States; Convergence Research Center for Energy and Environmental Sciences, Sungkyunkwan University, Suwon 16419, Korea; [orcid.org/0000-0003-0386-9118](https://orcid.org/0000-0003-0386-9118); Email: [yeonsign@uci.edu](mailto:yeonsign@uci.edu)

**Jin Yong Lee** – Convergence Research Center for Energy and Environmental Sciences, Sungkyunkwan University, Suwon 16419, Korea; Department of Chemistry, Sungkyunkwan University, Suwon 16419, Korea; [orcid.org/0000-0003-0360-5059](https://orcid.org/0000-0003-0360-5059); Email: [jinylee@skku.edu](mailto:jinylee@skku.edu)

**Artur Nenov** – Dipartimento di Chimica Industriale "Toso Montanari", Università degli Studi di Bologna, I-40136 Bologna, Italy; [orcid.org/0000-0003-3071-5341](https://orcid.org/0000-0003-3071-5341); Email: [artur.nenov@unibo.it](mailto:artur.nenov@unibo.it)

**Shaul Mukamel** – Department of Chemistry, University of California, Irvine, California 92697-2025, United States; [orcid.org/0000-0002-6015-3135](https://orcid.org/0000-0002-6015-3135); Email: [smukamel@uci.edu](mailto:smukamel@uci.edu)

### Authors

**Francesco Montorsi** – Dipartimento di Chimica Industriale "Toso Montanari", Università degli Studi di Bologna, I-40136 Bologna, Italy

**Daniel Keefer** – Department of Chemistry, University of California, Irvine, California 92697-2025, United States; [orcid.org/0000-0001-5941-5567](https://orcid.org/0000-0001-5941-5567)

**Stefano M. Cavalletto** – Department of Chemistry, University of California, Irvine, California 92697-2025, United States; [orcid.org/0000-0003-1516-7519](https://orcid.org/0000-0003-1516-7519)

**Marco Garavelli** – Dipartimento di Chimica Industriale "Toso Montanari", Università degli Studi di Bologna, I-40136 Bologna, Italy; [orcid.org/0000-0002-0796-289X](https://orcid.org/0000-0002-0796-289X)

Complete contact information is available at: <https://pubs.acs.org/doi/10.1021/acs.jctc.2c00064>

### Author Contributions

<sup>†</sup>Y.N. and F.M. contributed equally to this work.

### Notes

The authors declare no competing financial interest.

## ACKNOWLEDGMENTS

This work was primarily supported by the U.S. Department of Energy, Office of Science, Office of Basic Energy Sciences under Award DE-SC0019484 (S.M. and M.G.). The support of the National Science Foundation through Grant No. CHE-1953045 is gratefully acknowledged. Y.N. acknowledges support from the Korea Initiative for fostering University of Research and Innovation Program of the National Research

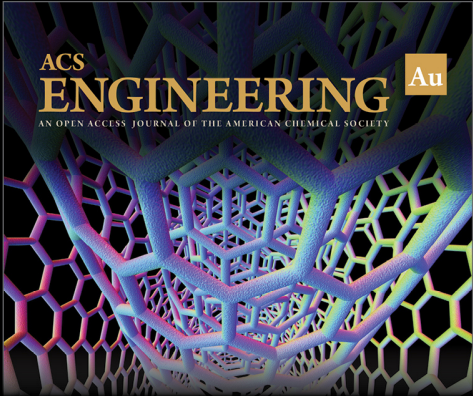
Foundation (NRF) funded by the Korean government (MSIT) (No. 2020M3H1A1077095). D.K. gratefully acknowledges support from the Alexander von Humboldt Foundation through the Feodor Lynen program.

## REFERENCES

- (1) Maiuri, M.; Garavelli, M.; Cerullo, G. Ultrafast Spectroscopy: State of the Art and Open Challenges. *J. Am. Chem. Soc.* **2020**, *142*, 3–15.
- (2) Conti, I.; Cerullo, G.; Nenov, A.; Garavelli, M. Ultrafast Spectroscopy of Photoactive Molecular Systems from First Principles: Where We Stand Today and Where We Are Going. *J. Am. Chem. Soc.* **2020**, *142*, 16117–16139.
- (3) Buchner, F.; Nakayama, A.; Yamazaki, S.; Ritze, H.-H.; Lübcke, A. Excited-State Relaxation of Hydrated Thymine and Thymidine Measured by Liquid-Jet Photoelectron Spectroscopy: Experiment and Simulation. *J. Am. Chem. Soc.* **2015**, *137*, 2931–2938.
- (4) Brister, M. M.; Crespo-Hernández, C. E. Excited-State Dynamics in the RNA Nucleotide Uridine 5-Monophosphate Investigated Using Femtosecond Broadband Transient Absorption Spectroscopy. *J. Phys. Chem. Lett.* **2019**, *10*, 2156–2161.
- (5) Erickson, B. A.; Heim, Z. N.; Pieri, E.; Liu, E.; Martinez, T. J.; Neumark, D. M. Relaxation Dynamics of Hydrated Thymine, Thymidine, and Thymidine Monophosphate Probed by Liquid Jet Time-Resolved Photoelectron Spectroscopy. *J. Phys. Chem. A* **2019**, *123*, 10676–10684.
- (6) Borrego-Varillas, R.; Nenov, A.; Kabaciński, P.; Conti, I.; Ganzer, L.; Oriana, A.; Jaiswal, V.; Delfino, I.; Weingart, O.; Manzoni, C.; Rivalta, I.; Garavelli, M.; Cerullo, G. Tracking excited state decay mechanisms of pyrimidine nucleosides in real time. *Nat. Commun.* **2021**, *12*, No. 7285.
- (7) Sánchez-Rodríguez, J. A.; Mohamadzade, A.; Mai, S.; Ashwood, B.; Pollum, M.; Marquetand, P.; González, L.; Crespo-Hernández, C. E.; Ullrich, S. 2-Thiouracil intersystem crossing photodynamics studied by wavelength-dependent photoelectron and transient absorption spectroscopies. *Phys. Chem. Chem. Phys.* **2017**, *19*, 19756–19766.
- (8) Mai, S.; Mohamadzade, A.; Marquetand, P.; González, L.; Ullrich, S. Simulated and Experimental Time-Resolved Photoelectron Spectra of the Intersystem Crossing Dynamics in 2-Thiouracil. *Molecules* **2018**, *23*, No. 2836.
- (9) Borrego-Varillas, R.; Teles-Ferreira, D. C.; Nenov, A.; Conti, I.; Ganzer, L.; Manzoni, C.; Garavelli, M.; Maria de Paula, A.; Cerullo, G. Observation of the Sub-100 Femtosecond Population of a Dark State in a Thiobase Mediating Intersystem Crossing. *J. Am. Chem. Soc.* **2018**, *140*, 16087–16093.
- (10) Teles-Ferreira, D. C.; Conti, I.; Borrego-Varillas, R.; Nenov, A.; Van Stokkum, I. H. M.; Ganzer, L.; Manzoni, C.; de Paula, A. M.; Cerullo, G.; Garavelli, M. A Unified Experimental/Theoretical Description of the Ultrafast Photophysics of Single and Double Thionated Uracils. *Chem. Eur. J.* **2020**, *26*, 336–343.
- (11) Pollum, M.; Lam, M.; Jockusch, S.; Crespo-Hernández, C. E. Dithionated Nucleobases as Effective Photodynamic Agents against Human Epidermoid Carcinoma Cells. *ChemMedChem* **2018**, *13*, 1044–1050.
- (12) Meisenheimer, K. M.; Koch, T. H. Photocross-Linking of Nucleic Acids to Associated Proteins. *Crit. Rev. Biochem. Mol. Biol.* **1997**, *32*, 101–140.
- (13) Favre, A.; Moreno, G.; Blondel, M.; Kliber, J.; Venzens, F.; Salet, C. 4-thiouridine photosensitized RNA-protein crosslinking in mammalian cells. *Biochem. Biophys. Res. Commun.* **1986**, *141*, 847–854.
- (14) Reichardt, C.; Guo, C.; Crespo-Hernández, C. E. Excited-State Dynamics in 6-Thioguanosine from the Femtosecond to Microsecond Time Scale. *J. Phys. Chem. B* **2011**, *115*, 3263–3270.
- (15) Pellegrini, C.; Marinelli, A.; Reiche, S. The physics of x-ray free-electron lasers. *Rev. Mod. Phys.* **2016**, *88*, No. 015006.
- (16) Chergui, M.; Collet, E. Photoinduced Structural Dynamics of Molecular Systems Mapped by Time-Resolved X-ray Methods. *Chem. Rev.* **2017**, *117*, 11025–11065.
- (17) Chen, L. X.; Zhang, X. Photochemical Processes Revealed by X-ray Transient Absorption Spectroscopy. *J. Phys. Chem. Lett.* **2013**, *4*, 4000–4013.
- (18) Chen, L. X.; Zhang, X.; Shelby, M. L. Recent advances on ultrafast X-ray spectroscopy in the chemical sciences. *Chem. Sci.* **2014**, *5*, 4136–4152.
- (19) Attar, A. R.; Bhattacharjee, A.; Pemmaraju, C. D.; Schnorr, K.; Closser, K. D.; Prendergast, D.; Leone, S. R. Femtosecond x-ray spectroscopy of an electrocyclic ring-opening reaction. *Science* **2017**, *356*, 54–59.
- (20) Bhattacharjee, A.; Pemmaraju, C. D.; Schnorr, K.; Attar, A. R.; Leone, S. R. Ultrafast Intersystem Crossing in Acetylacetone via Femtosecond X-ray Transient Absorption at the Carbon K-Edge. *J. Am. Chem. Soc.* **2017**, *139*, 16576–16583.
- (21) Neville, S. P.; Chergui, M.; Stolow, A.; Schuurman, M. S. Ultrafast X-Ray Spectroscopy of Conical Intersections. *Phys. Rev. Lett.* **2018**, *120*, 243001.
- (22) Yang, J.; Zhu, X.; Wolf, T. J. A.; et al. Imaging CF<sub>3</sub>I conical intersection and photodissociation dynamics with ultrafast electron diffraction. *Science* **2018**, *361*, 64–67.
- (23) Zinchenko, K. S.; Ardana-Lamas, F.; Seidu, I.; Neville, S. P.; Van Der Veen, J.; Lanfalonì, V. U.; Schuurman, M. S.; Wöner, H. J. Sub-7-femtosecond conical-intersection dynamics probed at the carbon K-edge. *Science* **2021**, *371*, 489.
- (24) Hua, W.; Mukamel, S.; Luo, Y. Transient X-ray Absorption Spectral Fingerprints of the S1 Dark State in Uracil. *J. Phys. Chem. Lett.* **2019**, *10*, 7172–7178.
- (25) Wolf, T. J. A.; Myhre, R. H.; Cryan, J. P.; et al. Probing ultrafast  $\pi\pi^*/n\pi^*$  internal conversion in organic chromophores via K-edge resonant absorption. *Nat. Commun.* **2017**, *8*, No. 29.
- (26) Nam, Y.; Keefer, D.; Nenov, A.; Conti, I.; Aleotti, F.; Segatta, F.; Lee, J. Y.; Garavelli, M.; Mukamel, S. Conical Intersection Passages of Molecules Probed by X-ray Diffraction and Stimulated Raman Spectroscopy. *J. Phys. Chem. Lett.* **2021**, *12*, 12300–12309.
- (27) Campbell, J.; Papp, T. Widths of the Atomic K-N7 Levels. *At. Data Nucl. Data Tables* **2001**, *77*, 1–56.
- (28) Mukamel, S.; Rahav, S. *Advances in Atomic, Molecular, and Optical Physics*; Arimondo, E.; Berman, P.; Lin, C., Eds.; Academic Press, 2010; Vol. 59, pp 223–263.
- (29) Finley, J.; Malmqvist, P.-Å.; Roos, B. O.; Serrano-Andrés, L. The multi-state CASPT2 method. *Chem. Phys. Lett.* **1998**, *288*, 299–306.
- (30) Forsberg, N.; Åke Malmqvist, P. Multiconfiguration perturbation theory with imaginary level shift. *Chem. Phys. Lett.* **1997**, *274*, 196–204.
- (31) Ghigo, G.; Roos, B. O.; Malmqvist, P.-Å. A modified definition of the zeroth-order Hamiltonian in multiconfigurational perturbation theory (CASPT2). *Chem. Phys. Lett.* **2004**, *396*, 142–149.
- (32) Widmark, P.-O.; Malmqvist, P.-Å.; Roos, B. O. Density matrix averaged atomic natural orbital (ANO) basis sets for correlated molecular wave functions. *Theor. Chim. Acta* **1990**, *77*, 291–306.
- (33) Malmqvist, P. A.; Rendell, A.; Roos, B. O. The restricted active space self-consistent-field method, implemented with a split graph unitary group approach. *J. Phys. Chem. V* **1990**, *94*, S477–S482.
- (34) Delcey, M. G.; Sørensen, L. K.; Vacher, M.; Couto, R. C.; Lundberg, M. Efficient calculations of a large number of highly excited states for multiconfigurational wavefunctions. *J. Comput. Chem.* **2019**, *40*, 1789–1799.
- (35) Sauri, V.; Serrano-Andrés, L.; Shahi, A. R. M.; Gagliardi, L.; Vancoillie, S.; Pierloot, K. Multiconfigurational Second-Order Perturbation Theory Restricted Active Space (RASPT2) Method for Electronic Excited States: A Benchmark Study. *J. Chem. Theory Comput.* **2011**, *7*, 153–168.
- (36) Almlöf, J.; Taylor, P. R. General contraction of Gaussian basis sets. I. Atomic natural orbitals for first- and second-row atoms. *J. Chem. Phys.* **1987**, *86*, 4070–4077.





- (37) Roos, B. O.; Lindh, R.; Malmqvist, P.-Å.; Veryazov, V.; Widmark, P.-O. New Relativistic ANO Basis Sets for Transition Metal Atoms. *J. Phys. Chem. A* **2005**, *109*, 6575–6579.
- (38) Segatta, F.; Russo, M.; Nascimento, D. R.; Presti, D.; Rigodanza, F.; Nenov, A.; Bonvicini, A.; Arcioni, A.; Mukamel, S.; Maiuri, M.; Muccioli, L.; Govind, N.; Cerullo, G.; Garavelli, M. In Silico Ultrafast Nonlinear Spectroscopy Meets Experiments: The Case of Perylene Bisimide Dye. *J. Chem. Theory Comput.* **2021**, *17*, 7134–7145.
- (39) Fdez Galván, I.; Vacher, M.; Alavi, A.; et al. OpenMolcas: From Source Code to Insight. *J. Chem. Theory Comput.* **2019**, *15*, 5925–5964.
- (40) Weingart, O.; Nenov, A.; Altoè, P.; Rivalta, I.; Segarra-Martí, J.; Dokukina, I.; Garavelli, M. COBRAMM 2.0 – A software interface for tailoring molecular electronic structure calculations and running nanoscale (QM/MM) simulations. *J. Mol. Model.* **2018**, *24*, No. 271.
- (41) Reiter, S.; Keefer, D.; de Vivie-Riedle, R. *Quantum Chemistry and Dynamics of Excited States*; John Wiley & Sons, Ltd., 2020; Chapter 11, pp 355–381.
- (42) Tal-Ezer, H.; Kosloff, R. An accurate and efficient scheme for propagating the time dependent Schrödinger equation. *J. Chem. Phys.* **1984**, *81*, 3967–3971.
- (43) Thallmair, S.; Roos, M. K.; de Vivie-Riedle, R. Design of specially adapted reactive coordinates to economically compute potential and kinetic energy operators including geometry relaxation. *J. Chem. Phys.* **2016**, *144*, No. 234104.
- (44) Butterworth, S. On the Theory of Filter Amplifiers *Experimental Wireless and the Wireless Engineer* 1930, *7*, 536–541.
- (45) Bhattacharjee, A.; Schnorr, K.; Oesterling, S.; Yang, Z.; Xue, T.; de Vivie-Riedle, R.; Leone, S. R. Photoinduced Heterocyclic Ring Opening of Furfural: Distinct Open-Chain Product Identification by Ultrafast X-ray Transient Absorption Spectroscopy. *J. Am. Chem. Soc.* **2018**, *140*, 12538–12544.




ACS  
**ENGINEERING** Au  
AN OPEN ACCESS JOURNAL OF THE AMERICAN CHEMICAL SOCIETY

Editor-in-Chief: **Prof. Shelley D. Minteer**, University of Utah, USA

 Deputy Editor:  
**Prof. Vivek Ranade**  
University of Limerick, Ireland

**Open for Submissions** 

pubs.acs.org/engineeringau  ACS Publications  
Most Trusted. Most Cited. Most Read.

-Supporting Information-  
Time-Resolved Optical-Pump, Resonant X-ray Probe  
Spectroscopy of 4-Thiouracil; a Simulation Study

Yeonsig Nam<sup>1,2,\*,†</sup>, Francesco Montorsi<sup>3,†</sup>, Daniel Keefer<sup>1</sup>, Stefano M. Cavaletto<sup>1</sup>,  
Jin Yong Lee<sup>2,4\*</sup>, Artur Nenov<sup>3\*</sup>, Marco Garavelli<sup>3</sup>, and Shaul Mukamel<sup>1\*</sup>

<sup>1</sup>Department of Chemistry, University of California, Irvine, California  
92697-2025, United States

<sup>2</sup>Convergence Research Center for Energy and Environmental Sciences,  
Sungkyunkwan University, Suwon 16419, Korea

<sup>3</sup>Dipartimento di Chimica Industriale "Toso Montanari," Università degli Studi  
di Bologna, I-40136 Bologna, Italy

<sup>4</sup>Department of Chemistry, Sungkyunkwan University, Suwon 16419, Korea

<sup>†</sup>These authors contribute equally to this work.

# Contents

Contents	S2
1 Loop Diagram Rules	S3
2 Supplementary Figures	S4



## 1 Loop Diagram Rules

The loop diagram of the optical pump - resonant X-ray probe signal is shown in Scheme 1b in the main manuscript and Figure S6. The Diagram rules are as follows:

- Time runs along the loop clockwise from bottom left to bottom right.
- Each field interaction is represented by an arrow, which either points to the right (photon annihilation and excitation of the molecule) or to the left (photon creation and de-excitation of the molecule).
- Free evolution periods on the left branch indicate forward propagation in real time, and on the right branch to backward propagation respectively.
- The last field interaction is the detected photon mode. In addition, the gray bar represents the period of free evolution.

## 2 Supplementary Figures

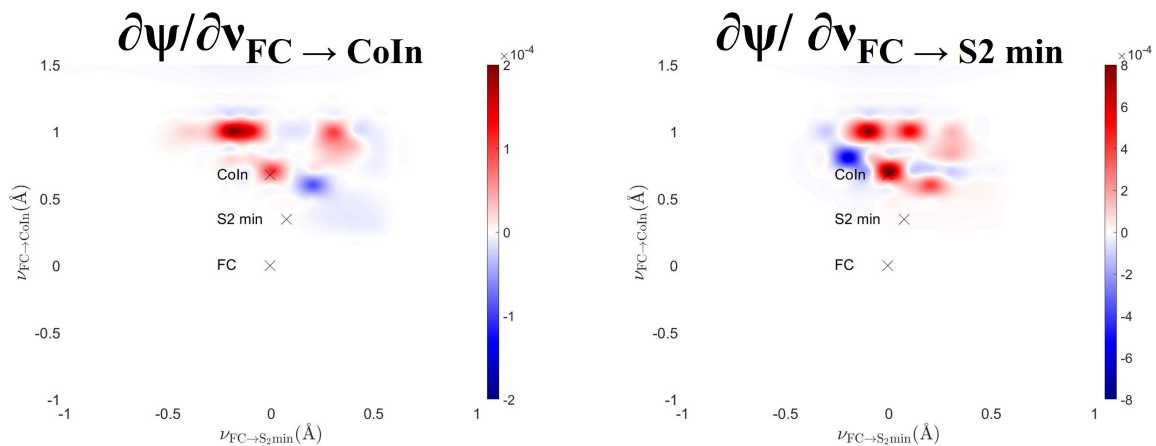


Figure S 1: Nonadiabatic couplings versus the two nuclear coordinates of the 4-thiouracil. The location of the FC, CoIn, and S2 min are marked with X. The spiky nature due to the phase change across the CoIn is observed.

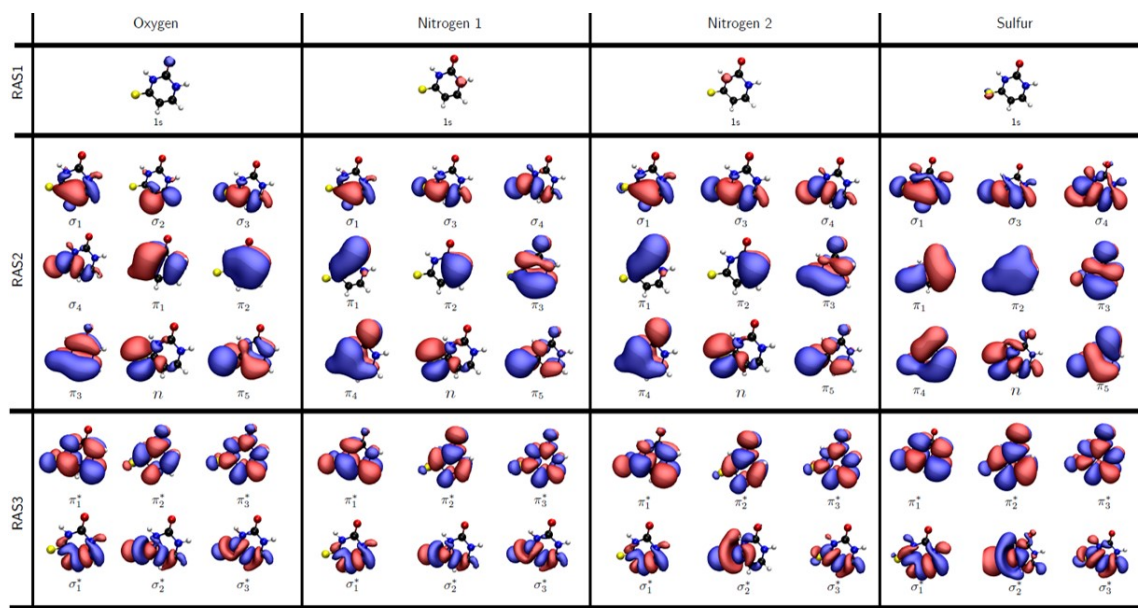


Figure S 2: CASSCF(20,16) active space. Active space for 4-thiouracil at the optimized ground state at the MP2 level (20 electrons in 16 orbitals) averaged over 3 lowest valence states,  $S_0 - S_2$  and 30 core states for each sulfur and 10 core states for oxygen and nitrogen K-edges.

Figure S 3: The nuclear wavepacket molecular dynamics movie on  $S_2$ ,  $S_1$ , and  $S_0$  PES.  $S_2$  wavepacket (gray contours),  $S_1$  wavepacket (pink contour), and  $S_0$  wavepacket (black contour). The location of the FC,  $S_2$  min, and CoIn is marked with "X". The pump-probe time-delay and the populations are shown in the bottom left corner. see the attached movie

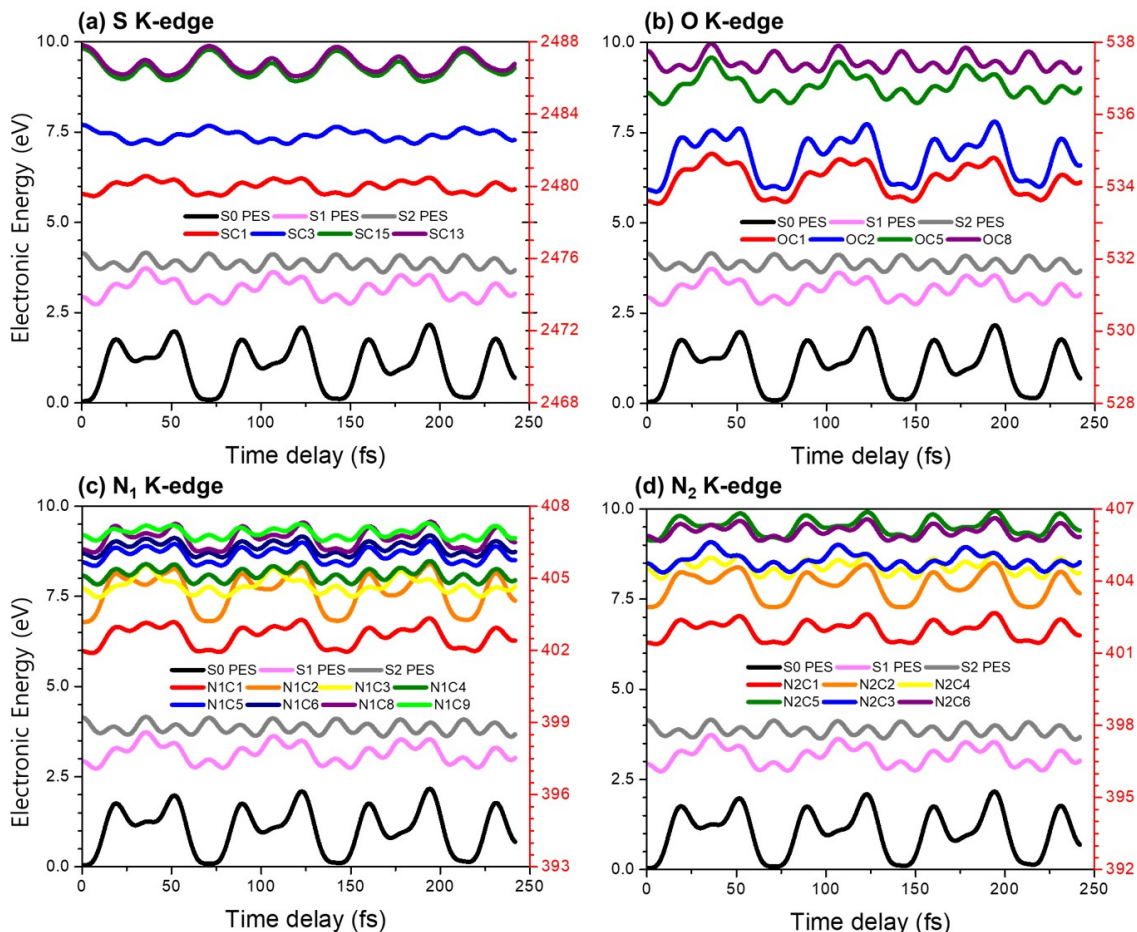
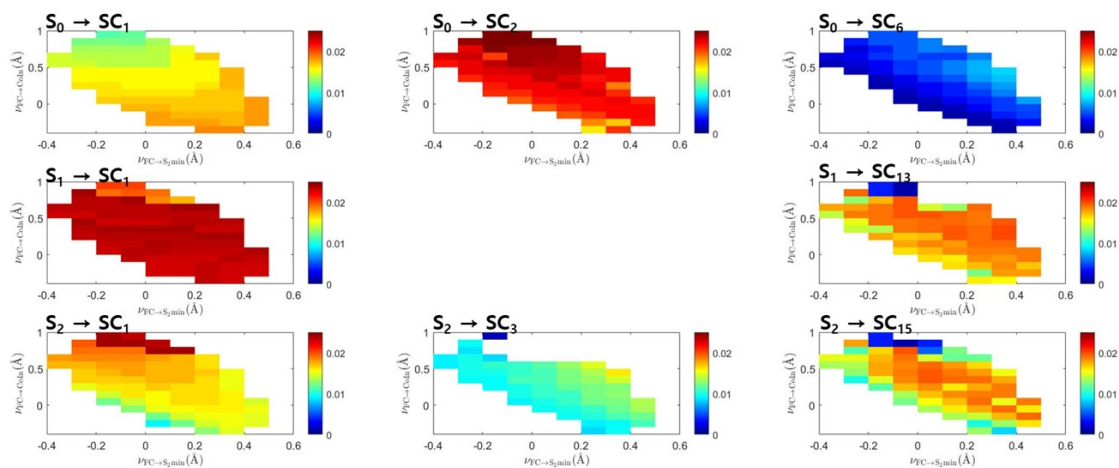


Figure S 4: Time-evolving electronic states levels for (a) S, (b) O, (c)  $N_1$ , and (d)  $N_2$  K-edges. The valence states,  $S_0$ ,  $S_1$ , and  $S_2$  are shown in black, pink, and gray lines, respectively. See the left y-axis for the valence energy levels and the right y-axis for the core energy levels.

**(a) S K-edge**



**(b) O K-edge**

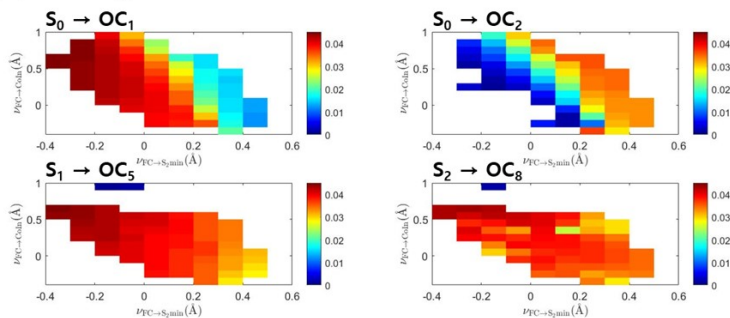


Figure S 5: Transition dipole moment between valence ( $S_0$ ,  $S_1$ , and  $S_2$ ) and core states over two-dimensional nuclear grids. (a) sulfur, (b) oxygen, and (c) nitrogen K-edges. Profiles pertaining to the same heteroatom are plotted in the same [min:max] range to allow easier comparison.



(c) N K-edge

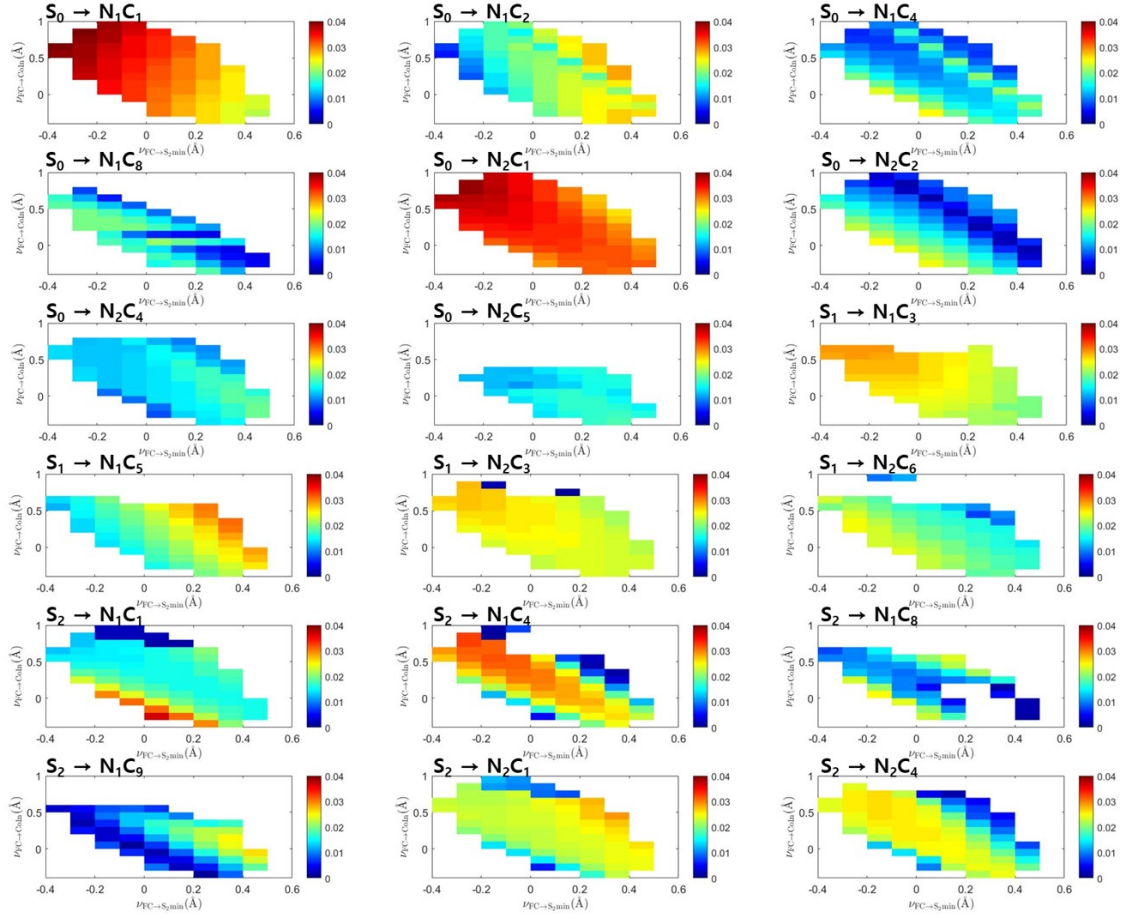


Figure S 5: (continued)

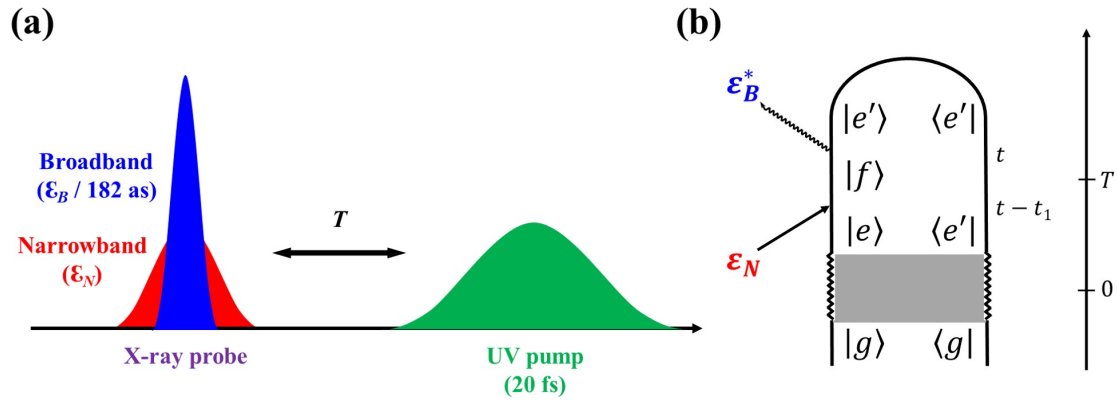


Figure S 6: (a) Pulse configuration for X-ray narrowband/broadband hybrid probe pulse and (b) the relevant Loop diagram. A hybrid X-ray field  $\mathcal{E}_B$  (broad) and  $\mathcal{E}_N$  (narrow) is used instead of a single broadband pulse that interacts twice. An incoming X-ray pulse ( $\mathcal{E}_N$ ) excites a molecule on a valence electronic surface  $|e\rangle$  into a core level  $|f\rangle$  after time delay  $T$  following an initial excitation into a non-stationary state and free evolution period (gray box). The signal field emission is stimulated by a broadband attosecond X-ray pulse ( $\mathcal{E}_B$ ).